Science Advances
AAAS

Manuscript Template

FRONT MATTER
ARTICLE TYPE: Research Articles

Title

- The source and accumulation of anthropogenic carbon in the U.S. East Coast

Short title: Anthropogenic carbon in the U.S. East Coast

Authors

Xinyu Li,[1,2] Zelun Wu,[1,3] Zhangxian Ouyang,[1] Wei-Jun Cai[1*]

Affiliations

[1] School of Marine Science and Policy, University of Delaware, Newark, Delaware, 19716, USA

[2] The Cooperative Institute for Climate, Ocean, and Ecosystem Studies, Seattle, Washington, 98105, USA

[3] College of Ocean and Earth Science, Xiamen University, Xiamen, Fujian, 361102, China

*Corresponding author, email: wcai@udel.edu

Abstract

The ocean has absorbed anthropogenic carbon dioxide (C_{anthro}) from the atmosphere and played an important role in mitigating global warming. However, how much C_{anthro} is accumulated in coastal oceans and where it comes from have rarely been addressed with observational data. Here, we use a high-quality carbonate dataset (1996-2018) in the U.S. East Coast to address these questions. Our work shows that the offshore slope waters have the highest C_{anthro} accumulation rates (ΔC_{anthro}) consistent with water mass age and properties. From offshore to nearshore, ΔC_{anthro} decreases with salinity to near zero in the subsurface, indicating no net increase in the export of C_{anthro} from estuaries and wetlands. The conservative mixing baseline also reveals an uptake of C_{anthro} from the atmosphere within the shelf. Our analysis suggests that the continental shelf exports most of its absorbed C_{anthro} from the atmosphere to the open ocean and acts as an essential pathway for global ocean C_{anthro} storage and acidification.

Teaser

Continental shelves export anthropogenic carbon absorbed from the atmosphere but receive nearly zero from estuaries.

Continental shelves receive little anthropogenic carbon from estuaries but transport it from the atmosphere to the open ocean.

MAIN TEXT

Introduction

The ocean's overall role as a sink for anthropogenic carbon (C_{anthro}) has been determined unequivocally via global air-sea carbon dioxide (CO_2) flux observations(*1*), global oceanic anthropogenic carbon inventory observations(*2–6*), and ocean physical-biogeochemical model simulations(*7*, *8*). As such the ocean has played an important role in shouldering CO_2 storage and mitigating global warming but also has suffered from the acidification stress resulting from the absorbed CO_2(*9*, *10*). However, it has not yet been revealed how much C_{anthro} accumulated in the coastal ocean and where it comes from using observational data within coastal oceans.

Though small in surface area, the coastal regions, including estuaries, tidal wetlands, and the continental shelf and upper slope, are important locations for global carbon budget with high variability and uncertainty due to the heterogeneity within and among coastal systems (*11–13*). After two decades of intensive field and modeling research, it is clear now that the continental shelf is presently a sink for atmospheric CO_2 while estuaries are a CO_2 source driven by both the river and wetland carbon export(*14*, *15*). Previous models and conceptual frameworks have suggested that the continental shelf is an increasing CO_2 sink, either switching from a source(*16*) or being enhanced from a weak sink in the preindustrial time to a stronger sink at present(*17*), implying the continental shelf as a potentially critical location to take up anthropogenic CO_2 and to export it to the open ocean(*18*, *19*). Recent syntheses of observational data and model results have determined that the global atmospheric CO_2 uptake rate is about 0.25 PgC yr^{-1} (*11*, *14*, *20*) for the continental shelf (to 200 m). However, so far, we have no evidence to conclude on how much of this contemporaneous CO_2 uptake flux is stored as C_{anthro}, though conceptual model, mass-balance analysis, and numerical models often ignore coastal gradients and heterogeneities and suggest a substantial amount of the total flux is anthropogenic CO_2 uptake by the coastal ocean(*18*).

An even less known but immensely important question considers whether there is a lateral transport of anthropogenic carbon from the terrestrial system to the open ocean along the land-ocean aquatic continuum (LOAC). A recent analysis by Regnier et al.(*20*) has suggested that, globally, net C_{anthro} flux from the estuaries-wetlands to the continental shelf over the industrial period is essentially zero (0.05±0.10 PgC yr^{-1}). This is a downward revision of the LOAC C_{anthro} flux of about 0.1 PgC yr^{-1} previously proposed by Regnier et al. (2013) as it is believed to be compensated for by the more recent organic carbon loss in coastal wetlands (also see Dai et al. 2022(*15*)). However, the above conclusions are largely derived from indirect mass balance assessments and no direct observational evidence has been provided to support or negate them. In contrast, another model-based global river carbon budget analysis showed the carbon export from river to ocean (~0.9 PgC yr^{-1}, in which DIC is ~0.6 PgC yr^{-1}) has been stable, meaning no net C_{anthro}, during the 20th century(*21*). Furthermore, a recent global synthesis of riverine

bicarbonate (HCO_3^-) export is also inconclusive regarding whether anthropogenic activities have increased river HCO_3^- flux on a global scale(*22*), though other syntheses have suggested that part of the terrestrial organic carbon export could be converted to dissolved inorganic carbon (DIC) and together with the CO_2 uptake from the atmosphere, they have increased the shelf to open ocean export of DIC(*11*, *14*). In summary, the input and accumulation rates, variabilities, and controls of the C_{anthro} in coastal oceans are still unclear. An assessment based on direct observations of anthropogenic carbon accumulation in downstream coastal oceans may provide a new angle to address this unresolved question which is of broad interest to ocean and global carbon cycle and climate change communities.

To distinguish C_{anthro} from the natural background in the coastal ocean is challenging as only the total carbon changes can be directly measured and as the ratio of signal (anthropogenic trend) to noise (natural variability) may be small in coastal regions due to high natural variability and limited period of observational data(*8*, *23*). Hence coastal C_{anthro} estimation has so far mainly relied on either biogeochemical model simulations(*17*–*19*) or a combination of conceptual model understanding and mass-balance analysis(*19*, *20*). While attempts of estimating C_{anthro} have been made on large marginal sea basins such as the South China Sea(*24*, *25*) and the Mediterranean Sea(*26*), these isolated deep basins are treated like the open ocean basins, involving no data from low salinity shelf and nearshore waters. In addition, C_{anthro} content was also assessed in the upwelling dominated eastern boundary ocean margins(*27*, *28*), yet it was extrapolated from the decadal repeated carbonate observations of the open ocean to the coastal waters(*29*, *30*). While C_{anthro} was also estimated and its impact on acidification was assessed in nearshore systems, such studies were generally limited to surface (*31*, *32*) or seasonally hypoxic shallow subsurface water(*33*). Thus, high-quality synoptic coastal cruise data have barely been used to estimate regional C_{anthro} directly so far. Although using the high-quality and long-term carbonate parameter observational data within shallow coastal oceans is the preferred path to move forward, time-series investigations of accurate and precise carbonate parameters of sufficiently long periods (> two decades) are rare in coastal ocean. To our knowledge, the North American East Coast may be the only ocean margin, among those seriously impacted by terrestrial carbon exports, which meets the criteria with a time series of high-quality carbonate chemistry investigations that can be traced back more than 20 years to the mid-1990s(*34*–*37*).

Here, we take advantage of such a dataset from 1996 to 2018 to estimate the C_{anthro} change (ΔC_{anthro}) and explore its controlling processes in the U.S. Mid-Atlantic Bight (MAB) (fig. S1). Our results show that ΔC_{anthro} is nearly zero in the low salinity ($S<32$) nearshore waters, meaning no increase in the C_{anthro} export from estuaries-wetlands. We further conclude that only a small fraction of anthropogenic CO_2 uptake by the continental shelf has been stored within the shelf while the majority is exported to the open ocean, aligning with recent model results. These conclusions may have major implications for C_{anthro} re-distribution among the Earth systems. Our conclusions may stimulate a community-wide level effort to quantify coastal C_{anthro} storage rates as more and more high-quality and long-term carbonate parameter data become available in the

highly heterogeneous global coastal oceans in the next two decades, improve the constraint of boundary conditions in regional and global ocean carbon models, and potentially provide the necessary baseline for assessing the marine carbon dioxide removal (mCDR) intervenes.

Results

Dissolved inorganic carbon decadal changes

We first identified a consistent spatial distribution pattern and an evolving temporal change of DIC from 1996 to 2018 across five research cruises in the MAB (Fig. 1, fig. S1, table S1). The spatial variations of DIC content are largely determined by their source water properties (fig. S2 – S3). On the shelf, DIC concentrations are low in the low salinity nearshore water and the low salinity and cold shelf water from the alongshore Labrador Current (LC)(*38*, *39*) (Fig. 1A – 1C and fig. S2). DIC concentrations increase moving offshore, especially in waters proximity to the Gulf Stream (Fig. 1A and 1B and fig. S3). On the continental slope, DIC is low in the top 200m of the high-temperature and salinity Gulf Stream water (GS) (Fig.1 and fig. S2 – S3). At deeper depth, DIC concentration rises in the low oxygen and high silicate (fig. S3) Antarctic Intermediate Water plus other intermediate waters (AAIW+)(*34*) (Fig.1C). Additionally, high DIC content is also observed below 500 m in the upper branch of the North Atlantic Deep Water (uNADW)(*40*, *41*)(Fig. 1A – 1C).

DIC increases with time in the whole water column, extending from the southmost transect to the northmost transect (Fig. 1A, 1B and 1D), which is supported by a statistical analysis of both DIC and salinity normalized DIC in different water masses (fig. S4). DIC increasing trend is most distinct in the slope water (fig. S4, $r \geq 0.8$, $P \leq 0.1$), while DIC increases in nearshore waters are not statistically significant. In contrast, the contents of temperature, salinity, oxygen, and silicate exhibit large variations and do not show distinguishable secular changes with time in these coastal water masses from 1996 to 2018. (fig. S5, fig. S6 and table S2). However, due to the large natural variations, additional analysis is needed to isolate how much DIC changes is contributed from ΔC_{anthro}.

Anthropogenic carbon accumulations in slope waters

To identify the anthropogenic effect on the secular trends of DIC changes, we estimated ΔC_{anthro} and its increasing rate in the subsurface using a time series analysis of regional extended multiple linear regression (regional eMLR)(*42*, *43*) built from salinity, temperature, oxygen, and silicate concentration (Methods, table S3 and table S4). The results are further validated by the ensemble eMLR approach(*30*) (table S5 and table S6). While similar in principle to the eMLR approaches developed and used for the open ocean basins, regional eMLR includes a cross term to deal with the more dynamic coastal oceans(*42*, *43*). On the surface (depth < 20 m), we estimated ΔC_{anthro} using the constant

air-sea disequilibrium (ΔpCO_2 = seawater pCO_2 (pCO_{2sw}) – atmospheric pCO_2 (pCO_{2air})) method to avoid the pitfalls of the eMLR approach(*3*).

We found a strong ΔC_{anthro} vertical variation (Fig. 2A and 2B) in different slope water masses and distinct increasing trends with time (Fig. 2C). The highest ΔC_{anthro} (26 ± 2 µmol kg^{-1}) over the period of 22 years (or annual increasing rate of ~1.1± 0.1 µmol kg^{-1} yr^{-1}; table S6) is located in the top 200 m, where the water shows GS features with high salinity, temperature, and TA. Below the GS water, the lowest ΔC_{anthro} of 9 ± 3 µmol kg^{-1} (or annual increasing rate of 0.3 ± 0.1 µmol kg^{-1} yr^{-1}) is found in the AAIW+ water between 200 m to 500 m. Below 500 m, ΔC_{anthro} in the uNADW water is 16 ± 3 µmol kg^{-1} or an annual increasing rate of 0.5 ± 0.1 µmol kg^{-1} yr^{-1} (table S5 and S6).

This sandwich structure of ΔC_{anthro} in the slope water reflects the history and efficiency of the anthropogenic carbon uptake of the source waters, depending on the water-mass age (i.e., the time of last contact with the atmosphere) and water chemical properties. We illustrate and explain the mechanism on a $\Delta C_{anthro} - pCO_{2sw}$ space (Fig. 3) with the assumption that the air-sea CO_2 gradient, ΔpCO_2, in each source water has remained constant over the recent few decades(*3*). Here, each group of contours represents the ΔC_{anthro} corresponding to a historical atmospheric CO_2 increase in different water masses. On the slope, the GS water-mass age is within one year because it is in the surface and upper water column(*44*, *45*). Therefore, under full air-sea equilibrium, we estimated that the GS water with high salinity and TA should have taken up about 26 µmol kg^{-1} of ΔC_{anthro} between 1996 and 2018 when the pCO_{2air} increased from 363 to 408 ppm (Fig. 3, red circles and solid arrow), which is compatible with the eMLR-derived ΔC_{anthro} of ~26 ± 2 µmol kg^{-1} (table S5).

The deep uNADW, originated from the Labrador Sea by winter-time convection(*46*), takes about 18-22 years for the surface Labrador Sea water to subduct to 1000 m depth and move to the MAB region along isopycnals(*46*). Therefore, the uNADW ΔC_{anthro} accumulation signal from 1996 to 2018 actually reflected the air-sea exchange state of the Labrador Sea surface seawater around two decades before the respective survey times. Theoretically, ΔC_{anthro} accumulation in the uNADW should be about 16 µmol kg^{-1} for the 20-year period when pCO_{2air} increased from 330 ppm in 1976 to 364 ppm in 1998 (Fig. 3, the blue circles and solid arrow). However, not all uNADW in this region is newly convected(*46*), and thus the actual ΔC_{anthro} could be lower. Our eMLR-derived ΔC_{anthro} (16 ± 3 µmol kg^{-1}, table S5) from observational data closely matches this theoretical prediction within uncertainties. Finally, the AAIW+ water originated from the Antarctic has a water mass age of at least 50 years(*47*). As pCO_{2air} increase was small (~ 7 ppm or less) during a 22-year time span in the mid or early part of the 20th century(*48*), the ΔC_{anthro} accumulation rate is very low and indistinguishable from the uncertainty of estimation.

Anthropogenic carbon accumulations in shelf waters

For the shelf water (water depth < 200 m), we used the same approaches (regional eMLR approach in the subsurface and constant ΔpCO_2 method in the surface) to evaluate ΔC_{anthro}. We also tested other methods of estimating ΔC_{anthro} in the surface layer, though variance is shown in ΔC_{Anthro} content in low salinity water, they all generated similar distribution pattern and conclusions (Supplementary Material section 4). Vertically, we found that the ΔC_{anthro} is higher in the surface ($\sigma < 24$) than in the subsurface (Fig. 4A – 4D). Horizontally, the most distinguished feature is a decreasing ΔC_{anthro} from offshore to nearshore. Thus, both cross-shelf mixing and air-sea CO_2 exchange are important factors influencing the distribution of C_{anthro} in continental shelf waters.

The relationship between salinity and ΔC_{anthro} (Fig. 4E) can be used to separate water mass mixing and ΔC_{anthro} storage and to explore the mechanisms behind the complex distribution pattern of shelf water ΔC_{anthro}. Once a water parcel leaves the surface and is isolated from the atmosphere, its ΔC_{anthro} is mainly affected by the water's physical mixing and can be considered quasi-conservative. Thus, in the subsurface, a triangle shape distribution of ΔC_{anthro} against salinity (red triangle in Fig. 4E) indicates a three end-members mixing of the low-salinity nearshore water from estuaries, the mid-salinity southward alongshore LC water, and the high-salinity northward GS water. Interestingly, the two coastal end-members have distinctly different ΔC_{anthro} (fig. S7). The alongshore LC water has ΔC_{anthro} of 17 ± 4 µmol kg^{-1} (Fig. 4E, table S5), matching our theoretical ΔC_{anthro} estimation of ~19 µmol kg^{-1} from 1996 to 2018 at S = 33, T =10°C (Fig. 3, blue square). However, in stark contrast, the nearshore low salinity end-member originated from local estuaries and wetlands (S < 30, T = 25°C) has a near-zero ΔC_{anthro} (6 ± 7 µmol kg^{-1}, Fig. 4E and table S5) between 1996 and 2018, which greatly deviates from the ΔC_{anthro} estimation of 20 µmol kg^{-1} under air-sea gas equilibrium assumption.

A near-zero ΔC_{anthro} in the nearshore subsurface water from estuaries can first be attributed to two characteristics of its source water when it is on the surface: 1) high sea surface pCO_2 and low buffer capacity, and 2) short water residence time. We again illustrate and explain the control mechanism on the $C_{anthro} - pCO_{2sw}$ space (Fig. 3), focusing on surface water with high pCO_2. The increase of DIC caused by the same pCO_{2air} increase becomes smaller when the water pCO_{2sw} is higher and water's buffer capacity is lower (Fig. 3, represented by the changing slopes of the contours). For example, high seawater pCO_2 (500 ppm) in the low salinity nearshore water can only allow a small amount of ΔC_{anthro} accumulation (~12 µmol kg^{-1}) corresponding to the 45 ppm atmospheric CO_2 increase between 1996 and 2018 (Fig. 3, red squares and dark red solid arrow). In addition, the short water residence time also limits ΔC_{anthro} storage in the nearshore waters. Near the estuarine mouth, the water residence time is usually short (10 -100 days)(*49–51*), which causes a faster DIC exchange with the end-member waters (here we used a mixture of estuarine water and the offshore water). We simulated the effect of residence time using a simple 1-D box model, which assumes constant physical, chemical, and biological parameters but allows the pCO_{2air} to increase under a suite of different mixing scenarios from the marine-dominant case (10% estuarine and 90% marine) to the estuarine-dominant case (90% estuarine and 10% marine) (see Method, fig. S8). The simulation results illustrated that ΔC_{anthro} in 10-day and 100-day residence

time scenarios can accumulate only about 20% and 40%, respectively, of the ΔC_{anthro} values with the infinitely long residence time scenario derived from the estuarine-dominant case (Fig. 3, yellow and orange arrows, fig. S8).

In the surface water, the ΔC_{anthro}, though also decreasing with the salinity decrease, is higher than the subsurface ΔC_{anthro} in the low salinity end, which indicates that other than water-mass mixing, an extra source contributes to the surface water C_{anthro} (Fig. 4E). If we average the subsurface ΔC_{anthro} at the same salinity and consider it as a baseline from the conservative mixing of the open ocean water and a composite end-member of low salinity waters (Fig. 4E dashed red line), then the difference between the observed surface ΔC_{anthro} and the mixing line reflects the accumulated extra ΔC_{anthro} from local atmospheric CO_2 uptake within the shelf (Fig. 4E, black hollow arrow). We estimated that the volume-integrated surface mixed layer ΔC_{anthro} inventory change is about 0.018 Tg C yr^{-1} (or 0.6 mgC m^{-2} yr^{-1} if taking the averaged mixed layer depth as 20 m) in the MAB. Compared to the mixing line, the local air-sea gas exchange would contribute an additional 63 % anthropogenic CO_2 accumulation in the surface water (0.018-0.011)/0.011 × 100% = 63% where 0.011 Tg C yr^{-1} represents the conservative mixing baseline value).

Discussion

Our results provide the first solid evidence in constraining the anthropogenic carbon flux in the continental shelf realm based on the long-term oceanic observational dataset. This observational conclusion further clarifies and fortifies the existing continental shelf carbon budget analyses, previously only reliant on models, mass balance analysis, and conceptual frameworks.

First, the derived near-zero ΔC_{anthro} in the low salinity nearshore water (Fig. 4) indicates that the contribution of the ΔC_{anthro} from estuaries and wetlands to the shelf is rather limited. The ΔC_{anthro} could be negative when it is extrapolated to an even lower salinity (Fig. 4 and Fig. 5). This conclusion supports the mass balance analysis results of Regnier et al.(*20*) that net C_{anthro} flux from estuaries and wetlands to the continental shelf is essentially zero and can be negative (0.05±0.10 PgC yr^{-1}) as the riverine C_{anthro} flux (0.10±0.05 PgC yr^{-1}) is counter balanced by the reduced wetland area and its associated carbon loss and reduced CO_2 uptake from the atmosphere within the past few decades. This notion is supported by the report that the North America has a wetland loss rate 3 times of its growth rate(*52*). This conclusion is also consistent with another global river analysis which suggests no obvious change of riverine carbon export during the 20th century(*21*). The possibility of the estuaries being a site of reduced/removing C_{anthro} uptake requires additional independent assessments but, if proven to be true, it will have important ramifications for global carbon cycle studies under a changing climate, in particular in the context of current interest in considering coastal wetlands and estuaries zone as viable storage reservoirs for carbon dioxide removal (CDR)(*53*).

Another insight from our study worthy of further exploration is the fate of C_{anthro} from the local atmospheric CO_2 uptake. Here we first quantify that the volume-integrated total anthropogenic carbon inventory change rate is about 0.055 Tg C yr^{-1} in the MAB shelf,

which is only about 3.4% of total air-sea CO_2 uptake (1.6 Tg C yr^{-1}) (see Methods) (Fig. 5). Assuming that the air-sea C_{anthro} flux is 30% -70% of the total air-sea flux (*15*, *18*, *20*, *54*, *55*), then we can conclude that only 5% - 11% the air-sea C_{anthro} flux is accumulated in the water column and that the majority of C_{anthro} (89% - 95%) must be exported to the open ocean. Even if we take the perturbed particulate organic carbon (POC) burial estimations into consideration (10% - 22%, twice of the C_{anthro} in the water column)(*17*, *20*, *56*), the majority of C_{anthro} uptake (68% - 85%) would still be exported. This observation-based conclusion agrees with the model result of Bourgeois et al(*18*), though our export percentage is even higher (Fig. 5). We further simulated the C_{anthro} accumulated in the water and the C_{anthro} uptake from the atmosphere using the same 1-D box model assuming pCO_{2air} increase is the only driver under a suite of different mixing scenarios (See Method). The box model simulation also suggested that only 4% - 28% of C_{anthro} uptake through air-sea flux is accumulated within the shelf due to its limited volume and relatively short water residence time. The majority of this local gas-exchange-induced C_{anthro} (72% - 96%) is exported to the open ocean in the MAB (Fig. 5). Therefore, we further concluded that while the continental shelf is not efficient in accumulating C_{anthro}, it is highly efficient in exporting its locally absorbed anthropogenic CO_2 from the atmosphere to the open ocean and thus may play a critical role in the ocean acidification pathway.

Our observation-based findings address the questions of how and how much ΔC_{anthro} is accumulated in the coastal region and where it comes and goes, and substantiated recent assessments from numerical models, mass balance exercises, and conceptual frameworks. Our conclusions will also have implications for setting up or verifying boundary conditions in regional and global carbon cycle models and budgets(*57*). Though some previous studies have shown that C_{anthro} accumulations in coastal regions can be influenced by overturning circulations(*58*), water ventilation(*59*, *60*), upwelling(*61*) and water buffer capacity(*62*), our study specifically addresses the C_{anthro} accumulations mechanism in an open continental shelf with substantial influences from the terrestrial and estuarine sources and the open ocean. However, the coastal region is diverse and dynamic with local features. Consequently, accurately quantifying the contribution and storage percentage of ΔC_{anthro} in different types of continental shelves globally (F_{CS}, Fig. 5) remains challenging, given these complexities, but are highly needed. Our study only examined one example of using high-quality summer coastal cruises to conduct independent and high-resolution C_{anthro} estimation and inventory changes. The coastal cruises usually have higher temporal and spatial sampling frequency, which can reveal the region-specific C_{anthro} features and detect C_{anthro} evolution. The method established and validated in this study can potentially be used in different coastal regions and enhance the understanding of past, present, and future coastal C_{anthro} changes. Especially relevant and timely, the application of this method can benefit the understanding of coastal C_{anthro} dynamics, which is critical to evaluating and verifying the efficacy of the various marine CDR strategies in the following decades.

We also advocate that future research should quantify and understand the contributions of anomalous CO_2 fluxes (that is non-steady state changes) from estuaries to the continental shelf (F_{EC}, Fig. 5) (see Supplemental Material section 1 and 2) due to the changes in the

wetland area, nutrient concentration, increased chemical weathering under anthropogenic pressure and climate change stresses(*12*, *22*, *63*), and terrestrial organic and inorganic carbon inputs forced by hydrological cycle (e.g., wet vs. dry years, extreme events, damming and etc.(*64*)) and coastal currents, which may substantially alter the C_{anthro} accumulation in rates and status on a regional scale. For example, anthropogenic activities have increased the net fluxes/burial of mud-associated organic carbon in some coastal environment but probably lead to a net decrease in coastal wetlands(*52*, *64*). Even though most C_{anthro} estimations have assumed that C_{anthro} does not interact with organic carbon cycle (*65*), there are exceptions in this assumption, such as in the consideration of ocean acidification (OA) caused by the C_{anthro}, one also considers how OA modifies the natural carbon cycle and what are their synergistic impacts(*31*, *66–68*). This will need further clarification on whether the low ΔC_{anthro} from the estuarine has been transformed into other forms of carbon and stored within the estuaries before it is exported to the continental shelf. A further collection of long-term and high-quality observational data and improvement of realistic and high-resolution global and regional coastal ocean models, and development of methodology in quantifying the component of non-steady state carbon and its interaction with climate change trend are clearly needed to validate and improve our conclusions and implications. With more high-quality and comprehensive data available in coastal oceans in the coming decade, we will be able to piece together a more complete picture of the contributions of the coastal ocean in anthropogenic carbon storage, ocean acidification, the global carbon cycle.

Materials and Methods

1.Data source

We used data from five research cruises in the Mid-Atlantic Bight (MAB) conducted in the summer of 1996 (Ocean Margin Program, OMP Cruise, http://po.msrc.sunysb.edu/omp/)(*36*), 2007 (Gulf of Mexico Ecosystem and Carbon Cycle Cruise 1, GOMECC1, https://www.aoml.noaa.gov/ocd/gcc/GOMECC1/), 2012(Gulf of Mexico Ecosystem and Carbon Cycle Cruise 2, GOMECC2, https://www.aoml.noaa.gov/ocd/gcc/GOMECC2/), 2015 (East Coast Ocean Acidification Cruise 1, ECOA1), and 2018 (East Coast Ocean Acidification Cruise 2, ECOA2, https://www.aoml.noaa.gov/ocd/gcc/ECOA/) (fig. S1 and table S1). Except for the 1996 cruise, we are part of the team that collected the data under the auspice of the Ocean Acidification Program (OAP), National Oceanic and Atmospheric Administration (NOAA).

Samples for dissolved inorganic carbon (DIC), total alkalinity (TA), oxygen (O_2), and dissolved inorganic nutrients (nitrate and nitrite (N), phosphate (P), silicate (Si)) were sampled from Niskin bottles. Salinity, temperature, and pressure data were from conductivity, temperature, and depth (CTD) sensors. In this work, DIC samples were measured by coulometric titration and TA was measured by acidimetric titration using the open-cell titration method. DIC and TA were checked or calibrated daily against Certificated Reference materials from Dr. Andrew Dickson's laboratory at Scripps Institution of Oceanography. The overall uncertainties of DIC and TA measurements

were within 0.1%. The precision and accuracy details on all physical and chemical parameters sampled can be found in each cruise report and have been archived (https://www.ncei.noaa.gov/access/ocean-carbon-acidification-data-system-portal/).

We assessed the cruise-to-cruise measurement biases by comparing crossover deep stations (table S2) and by comparing the hydrographic parameters from the same water mass (fig. S5, S6). Since previous studies have proven that the GOMECC and ECOA cruise are consistent and comparable to the GLODAP data(*69*, *70*), we especially compared the deep stations from the OMP cruises with the GLODAP stations (depth >1000 m) within 1° × 1° grid and 200 m depth differences. The hydrographic data differences between OMP and GLODAP are similar to the comparison of deep stations between Coastal Ocean Data Analysis Production in North America (CODAP-NA) and GLODAP data. In the deep-water masses (AAIW+ and uNADW), we found no statistical differences except silicate concentrations. Sensitivity analysis shows that the differences in these hydrographic parameters have little influence on ΔC_{anthro} and thus do not undermine our conclusions (see Method Section 2.1).

2. Anthropogenic carbon changes (ΔC_{anthro}) determination

A critical concept of interpreting present ocean interior DIC storage is to divide it into natural and anthropogenic carbon components(*71*). The natural component is the ocean DIC pool ($C_{natural}$) that exists in preindustrial time while the anthropogenic component (C_{anthro}) represents the perturbation by human activities(*65*). For a DIC content difference (ΔDIC) between two times (t_1 and t_2), it includes the changes caused by the anthropogenic carbon increase (ΔC_{anthro}) alone and natural variability ($\Delta C_{natural}$)(*43*). Thus ΔC_{anthro} is defined as:

$$\Delta C_{anthro(t_2-t_1)} = DIC_{t_2} - DIC_{t_1} - \Delta C_{natural(t_2-t_1)} \quad (1)$$

Both ΔC_{anthro} and $\Delta C_{natural}$ can be further separated into steady-state and non-steady-state components(*72*). The steady-state components represent the change of DIC in the absence of climate variability(*73*) while the non-steady-state components emerges from varying climate yet atmospheric CO_2 is unchanged(*65*). Following this definition, the natural steady-state variation is assumed to be zero when a sufficiently long time is given(*73*) whereas the natural non-steady-state variation contributes the most of $\Delta C_{natural(t_2-t_1)}$. The steady-state ΔC_{anthro} is the direct ocean response of atmospheric CO_2 increase only while the non-steady-state is anthropogenic CO_2 modified by other the climate changes (See details in Supplemental Material session 1).

Most methods of C_{anthro} estimation only constrain the steady state component(*72*). However, ΔC_{anthro} from extended multiple linear regression (eMLR) method cannot be easily defined. This eMLR method is used in the subsurface and may capture some non-steady-state signals based on a study of model-generated synthetic data.(*73*) Notably, ΔC_{anthro} from eMLR depends on some important assumptions, e.g. constant coefficients of natural components, small hydrographic variability and etc., (see the discussion by analytical analysis on decomposing the coefficients of eMLR in Supplemental Material Section 1 and 2). We validate these assumptions with observation data during our application of eMLR (see details in Method 2.1). The surface ΔC_{anthro} calculation is more

challenging in the coastal regions as strong seasonality and air-sea gas exchange make the establishment of eMLR in the surface mixed layer difficult and the results not reliable. The observed ΔpCO_2 climatology change can only capture the overall DIC pool changes(*74*). The widely adopted constant DIC disequilibrium (ΔTCO_2) method and constant ΔpCO_2 method(*3*) can estimate the steady-state component but not include non-steady-state component (see detailed discussions in Method 2.2 and Supplemental Material Section 3 and 4).

All C_{anthro} methods have caveats, especially if they are applied in the coastal ocean. We expect that non-steady state component of ΔC_{anthro} would play a more important role in the coastal region relative to the open ocean, which can be influenced by the changes of nutrient concentration, biological process shifts, terrestrial organic and inorganic carbon inputs, chemical weathering under anthropogenic stress. We discussed the influences of these factors on subsurface and surface ΔC_{anthro} estimation in Supplemental Material Section 2 and Section 4, respectively. Therefore, we recommend careful evaluations of the methodology before using any C_{anthro} estimations in coastal regions.

2.1 Subsurface ΔC_{anthro} determination and uncertainty analysis

We determined the subsurface ΔC_{anthro} increase rate using a time series analysis on the ΔC_{anthro} calculated from the eMLR method with interaction term in the coastal region (regional eMLR)(*42*). The eMLR method has been broadly applied to the repeated transects in the open ocean(*29*, *30*, *75–77*). However, such a method has not been used to constrain ΔC_{anthro} in coastal areas due to limited long-term observations and complex natural processes that may mask part of the anthropogenic signals and lead to large uncertainties in the ΔC_{anthro} estimates. Recent papers in the coastal regions have successfully built regional multiple linear regression (MLR) with interaction terms that can reconstruct the carbonate parameters with a high coefficient of determination (R^2)(*78–82*), which provides a solid foundation to apply.

The first step of the regional eMLR method is to build regional MLR models separately for five different cruises from 1996 to 2018. Here, we built MLR models following the steps in Li et al(*70*). To avoid the collinearity among the predictor variables and their interaction terms, all terms that lead to variance inflation factors (VIF) > 10 were excluded from the model. The combinations of T, S, O_2 and Si were chosen as the predictor parameters to build the MLR function because they deliver the smallest VIF values. We excluded water depth < 20 m since the summertime mixed layer depth in the U.S. East Coast is less than 20 m(*83*). The lower limit was set at 2000 m because the residuals began to shift with a trend in the deep layer (Fig. S9) and model performance deteriorated. To perform the eMLR method among different cruises, all models in different cruises must have the same predictor terms in the model for all cruises and O_2×Si is the only interaction term. Therefore, the final model equation for all cruises is,

$$DIC_{(t_i)} = X_{(t_i)} C_{(t_i)} \quad (2)$$

$X_{(t_i)}$ represents the anomalies (measured values subtract the mean) of input matrix of hydrographic data (i.e., salinity, temperature, O_2, and Si) and $C_{(t_i)}$ is the matrix of intercepts and coefficients (table S3),

$$C_{(t_i)} = \left[\alpha_{(t_i)} \quad \beta_{1,(t_i)} \quad \beta_{2,(t_i)} \quad \beta_{3,(t_i)} \quad \beta_{4,(t_i)} \quad \gamma_{(t_i)}\right]^T \tag{3}$$

The final regression equation is,

$$\begin{aligned} DIC = {} & \alpha + \beta_1(T - T_m) + \beta_2(S - S_m) + \beta_3(O_2 - O_{2m}) + \beta_4(Si - Si_m) \\ & + \gamma(O_2 - O_{2m}) \times (Si - Si_m) \end{aligned} \tag{4}$$

where X_m values are the mean of each data group (table S4).

To perform eMLR, we set 1996 as the reference year (t_1). Thus, ΔC_{anthro} indicates the amount of anthropogenic carbon accumulated between any year (t_i) and the reference year (t_1),

$$\Delta C_{anthro,(t_i)} = X_{(t_i)}(C_{(t_i)} - C_{(t_1)}) \tag{5}$$

Here i = [2,3,4,5] represents the time point of 2007, 2012, 2015 and 2018 cruise. Then we conducted a regression of the time and ΔC_{anthro} to derive the increasing rate of ΔC_{anthro} in different water mass.

There are a few assumptions in the application of the eMLR method, e.g., no temporal changes of relationship between predictive and predicted parameters in the natural components, small differences in the residuals between any two MLRs, and limited effects of hydrographic parameter variation on ΔC_{anthro} estimation. We examined these assumptions of eMLR and re-confirmed their validity in our study areas by conducting uncertainty analyses (see more discussion in Supplemental Material, sections 1 and 2). We especially tested the influence of hydrographic parameter changes on anthropogenic carbon by setting 2018 (instead of 1996) as the reference year and calculated ΔC_{anthro} increase from 1996 to 2018 (Fig. S10). The ΔC_{anthro} increase in different water masses shows similar results as those from setting 1996 as the reference year (Fig. 2).

We quantitatively estimated the uncertainties in the ΔC_{anthro} that arose from the MLR and eMLR models. The uncertainties in the MLR models come from the statistical model, the measurement uncertainty of response carbonate parameters and inputs(*73*, *84–86*). We combined these errors as the square root of the sum to evaluate the overall uncertainties (E_{est})(*70*).

$$E_{est} = \sqrt{E_{response}^2 + E_{Input}^2 + E_{MLR}^2} \tag{6}$$

Here, $E_{response}$ represents DIC measurement uncertainties in the whole data set (0.1%). The E_{input} is the uncertainty of the input parameters propagated in the regression, which can be calculated as $\sqrt{\sum_{i=1}^{n}(U_i\beta_i)^2}$. U_i is the *i*-th input uncertainties of the predictor properties. We set the U_i values 0.005, 0.005°C, 1% and 2% for S, T, O_2, and Si respectively(*87*, *88*). The β_i terms are the *i*-th regression coefficients in the MLR models. E_{MLR} refers to the model root mean square error (table S3). In addition, we conducted a sensitivity analysis on how much the change of hydrographic data from time one to time two affects the ΔC_{anthro}. We used the mean differences of hydrographic parameters in AAIW+ and uNADW water among the five cruises as input sensitivity tests (Figure S5).

Besides, the sea surface T and S change in the MAB is about 0.2°C and 0.2 S(*89*, *90*). Our results suggest that changes of 0.2°C, 0.2 S, 10 µmol kg^{-1} of O_2, and 3 µmol kg^{-1} of Si correspond to a ΔC_{anthro} change of 1.6 ± 0.5 µmol kg^{-1}, 2.4 ± 0.4 µmol kg^{-1}, 3.0 ± 0.4 µmol kg^{-1} and 2.5± 1.9 µmol kg^{-1}, respectively.

We also tested the model robustness by substituting Si with N or P in the combination of predictors in the eMLR(*86*). We evaluated the mean ΔC_{anthro} (ensemble MLR method(*30*)) and compared the ΔC_{anthro} from different models to estimate the uncertainty ranges caused by the choice of different parameters (table S5 and Fig. S11). The ensemble eMLR also derived similar ΔC_{anthro} increase rates as shown in eMLR approach (table S6). Finally, to validate the overall accuracy of our algorithm, we applied our regional eMLR method to a dataset with known C_{anth} additions to test if it can capture the low C_{anthro} especially in the low salinity waters (Fig. S12).

2.2 Surface ΔC_{anthro} determination and uncertainty analysis

The surface ΔC_{anthro} calculation is more challenging in the coastal regions as strong seasonality and air-sea gas exchange make the establishment of eMLR in the surface mixed layer difficult. In the previous studies, several approaches are used for calculating surface ΔC_{anthro}: 1) Extend the eMLR coefficients derived from the subsurface layer to the surface(*91*); 2) Constant DIC disequilibrium (ΔTCO_2) method(*31*), and 3) Constant ΔpCO_2 method(*3*). In this paper, we adopted the constant ΔpCO_2 method because it takes the seawater initial pCO_2 and buffer capacity into consideration(*31*), especially in the nearshore regions where pCO_2 is high and mainly driven by biological fluxes(*92*, *93*). We also examined and compared with the surface ΔC_{anthro} derived from other methods (in the session and in Supplementary Material section 3 and 4).

For convenience, we start with known pCO2(t2), DIC(t2), and TA(t2) and estimate the CO2 state of in the past (t1). For the constant ΔpCO_2 method, we assumed that the gradient between pCO_{2sw} and pCO_{2air} is constant during the study period ($\Delta pCO_{2(t_1)} = \Delta pCO_{2(t_2)}$) under instantaneous equilibrium assumption. Thus, the estimated seawater pCO_2 at time t_1 is,

$$pCO_{2(t_1),sw,est} = pCO_{2(t_1),sw,eq} + \Delta pCO_{2(t_2)} \quad (7a)$$

Here, $pCO_{2(t1),\,sw,\,eq}$ is the surface seawater pCO_2 in equilibrium with the atmosphere at time t_1. The estimated DIC at time t_1 is calculated as,

$$DIC_{(t_1),est} = f(pCO_{2(t_1),sw,est}, TA_{(t_2)}) \quad (7b)$$

Then, ΔC_{anthro} in the surface layer is calculated as,

$$\Delta C_{anthro} = DIC_{(t_2),obs} - DIC_{(t_1),est} \quad (8)$$

where $DIC_{(t_2),obs}$ is the observed DIC at time t_2. The constant ΔpCO_2 assumption may not be validate for the coastal regions as suggested by previous studies (*16*, *17*) that the coastal regions, e.g., MAB, are a growing CO_2 sink. However, the 22-year time span is not long enough to detect the surface anthropogenic pCO_{2sw} signal changes based on the time of trend emergence analysis (Supplemental Materials, Section 3).We are aware that the constant ΔpCO_2 method is not perfect for mixed layer ΔC_{anthro} estimation and highly

influenced by the seasonality, yet it provides a credible range of ΔC_{anthro} in the surface layer and the uncertainty is assessed to be acceptable (Supplementary Material section 4).

In addition, we compared the surface ΔC_{anthro} estimations to two other approaches: 1) extending eMLR coefficients from subsurface to surface, and 2) constant ΔTCO_2 method. At high salinity end (S>35), all methods gave similar ΔC_{anthro} as the constant ΔpCO_2 method. At low salinity (S<32), we got smaller ΔC_{anthro} values when 1) extending eMLR coefficients from the subsurface (Fig. S13) and larger ΔC_{anthro} values when 2) applying constant ΔTCO_2 method (Fig. S13). The results of the constant ΔpCO_2 method fall within the range of the ΔTCO_2 method and that by extending eMLR coefficients to surface waters. Results from ΔTCO_2 delivered relative conservative results as it does not take seawater pCO_2 into consideration(*31*, *32*). ~~Note that if we use the constant ΔTCO_2 approach, the air-sea pCO_2 gradient and flux will become greater with time, whereas air-sea pCO_2 gradient and flux remain the same in the constant ΔpCO_2 (see Methods).~~ Nonetheless, all methods show a decreased ΔC_{anthro} from the open ocean towards the nearshore. Further details and estimations of surface ΔC_{anthro} from different methods can be found in the Supplemental Material section 4.

3. Carbon budget calculation

To quantify the C_{anthro} flux across the land-ocean interface, we calculated the coastal C_{anthro} accumulation inventory and air-sea gas total flux using observation data. The air-sea CO_2 flux of the MAB is calculated as follows(*94*):

$$F_{CO2} = kK_0(pCO_{2sw} - pCO_{2air}) \quad (9)$$

where $k = 0.251 \times U_{10} \times (Sc/660)^{-0.5}$ is the gas transfer velocity calculated from wind speed at 10 m (U_{10}) from ERA5 monthly averaged data on the sea surface (0.25° × 0.25° gridded, https://www.ecmwf.int/en/forecasts/datasets/reanalysis-datasets/era5) and the Schmidt number (Sc), K_0 is the CO_2 gas solubility(*95*). pCO_{2air} is calculated using CO_2 mole fractions (xCO_2, dry air) from the National Oceanic and Atmospheric Administration (NOAA) Greenhouse Gas Marine Boundary Layer Reference (MBL Reference, https://gml.noaa.gov/ccgg/mbl/mbl.html) by assuming saturated water vapor on the sea surface. The monthly climatology of F_{CO2} during 1996-2018 in the MAB is calculated and then averaged to annual climatology. The F_{CO2} climatology is multiplied by the surface area of the MAB (1.12×10^5 km^2) to get the total amount of CO_2 absorbed by the ocean.

We computed the ΔC_{anthro} inventory changes by multiplying ΔC_{anthro} by the shelf water volume. In the surface, we averaged the ΔC_{anthro} values at every 0.5 salinity interval and matched them to the decadal averaged surface summer data from World Ocean Atlas 2018 (WOA18, 0.25° × 0.25° gridded, standard depth interval, decadal periods of 1995-2017, https://www.ncei.noaa.gov/archive/accession/NCEI-WOA18). We took 20 m as the surface mixed layer depth (MLD)(*83*). For the subsurface, we linearly interpolate the ΔC_{anthro} in the dimension of T and S and then matched the interpolated ΔC_{anthro} to the grided decadal averaged summer T, S data from WOA18. Then, we summed all the grids together to calculate the subsurface C_{anthro} inventory changes. For the carbon inventory of

the box model, we simply interpolated the box modeled ΔC_{anthro} of different cases by S and matched them to the World Ocean Atlas S data.

4. Box Model simulations

To investigate the influence of residence time on the atmospheric CO_2 uptake and accumulation, we used an idealized 1-D model to simulate the ΔC_{anthro} accumulation in the continental shelf driven by the atmospheric CO_2 change. We assumed a constant rate of net community production (NCP) and constant physical mixing rates. Although such a simplified model cannot sufficiently simulate all observations, we expect the model to capture and illustrate the most important control mechanism in coastal ocean CO_2 uptake, storage, and export. The model included a coastal water box with various residence times (10 to 100 days), and two external sources: estuarine and open ocean inputs. The simulation steps, parameter choices and initial conditions are introduced below (Table S7).

We set the simulation time step as one day. For each time step, DIC concentration in the coastal box was calculated as,

$$\mathrm{DIC}_{t+1} = \mathrm{DIC}_t + \Delta\mathrm{DIC}_{t,(phy)} + \Delta\mathrm{DIC}_{t,(bio)} + \Delta\mathrm{DIC}_{t,(gas)} \quad (10)$$

where $\Delta\mathrm{DIC}_{t,(phy)}$, $\Delta\mathrm{DIC}_{t(bio)}$, and $\Delta\mathrm{DIC}_{t,(gas)}$ represent the DIC changes induced by physical mixing of riverine and marine end-members, net photosynthesis and respiration, and gas exchange, respectively. $\Delta\mathrm{DIC}_{i,(bio)}$and $\Delta\mathrm{DIC}_{i,(gas)}$ was calculated as,

$$\Delta\mathrm{DIC}_{t,(bio)} + \Delta\mathrm{DIC}_{t,(gas)} = (\mathrm{NCP} + F_{\mathrm{CO2,t}}) / \mathrm{MLD} \quad (11)$$

where the term $F_{\mathrm{CO2,t}}$ is calculated following Equation (9)(*94*) assuming a climatological wind speed of 5.0 m s^{-1} at 10 m and the NCP is set as 2 mmol C m^{-2} d^{-1} for the coastal box model as high respiration scenario(*96*). The mixed layer depth for the coastal ocean box model is set as 20 m(*83*). The atmospheric pCO_2 used throughout the simulation was converted from the adjusted xCO_2 change from 1996 to 2018.

It is difficult to calculate $\Delta\mathrm{DIC}_{t,(phy)}$ directly. Instead, we considered the physical mixing process as the water in the coastal box is replaced by a mixture of estuarine inputs and open ocean inputs at a rate of j % (j = 1, 2, 5, 10) water per day following the water renewal time.

$$\mathrm{DIC}_{t+1} = \mathrm{j}\ \%\ \mathrm{DIC}_{\mathrm{mix,t}} + (1 - \mathrm{j})\ \%\ (\mathrm{DIC}_t + \Delta\mathrm{DIC}_{t,(bio)} + \Delta\mathrm{DIC}_{t,(gas)}) \quad (12)$$

The $\mathrm{DIC}_{mix,t}$ is calculated as

$$\mathrm{DIC}_{\mathrm{mix,t}} = (f_{marine} * DIC_{marine,t} + f_{estuarine} * DIC_{estuarine}) \quad (13)$$

We set a series of different fractions of estuarine and marine end-member combinations (from $f_{marine} = 0.1$ to $f_{marine} = 0.9$) in the simulation (Fig. S8). $\mathrm{DIC}_{marine,t}$ was calculated from the open ocean end-member. We chose water with properties of T = 25°C, S= 36, TA = 2365 µmol kg^{-1} and pCO_2 = 360 ppm (Gulf Stream surface water) as the open ocean end-member. The open ocean end-member DIC changes were calculated following Eq (10), which was driven by atmospheric CO_2 increase under the condition of a balanced biological contribution (NCP) and physical mixing (i.e., CO_2 removal by

positive NCP and supply by mixing compensate each other). We assumed water exchange between coastal and open ocean water would not affect the open ocean water chemical properties because the open ocean volume is assumed infinitely large. We chose the water with T =20°C, S = 28, TA = 2079.4 µmol kg^{-1}, and pCO_2 = 500 ppm (general case, Table S7) as the estuarine end-member ($DIC_{estuarine}$) and presumed it to be unchanged and not influenced by the atmospheric CO_2 increase during the time of our concern due to low water buffer capacity and a small CO_2 outgassing. With the new DIC_{t+1}, a new $pCO_{2,\,t+1}$ was calculated with constant TA, T, S, and nutrients in CO2SYS (MATLAB version(*97*)). The new $pCO_{2,\,t+1}$ is substituted into the simulation iteration to calculate $\Delta DIC_{t,(gas)}$ in the next time step.

In addition, we ran another two sets of simulations with different estuarine pCO_2 values: an extremely high sea surface pCO_2 scenario (700 ppm) representing small estuaries like Hudson River and a relatively low pCO_2 scenario (400 ppm) representing the large estuaries like Chesapeake Bay in the MAB (Fig. S14 and Table S7). All simulation results indicated that fast mixing processes and short residence time restrains sea surface pCO_2 increase in the coastal box at a rate slower than both the atmospheric CO_2 and open ocean box pCO_2 increase (Fig. S8 and Fig. S14).

References

1. T. Takahashi, S. C. Sutherland, R. Wanninkhof, C. Sweeney, R. A. Feely, D. W. Chipman, B. Hales, G. Friederich, F. Chavez, C. Sabine, A. Watson, D. C. E. Bakker, U. Schuster, N. Metzl, H. Yoshikawa-Inoue, M. Ishii, T. Midorikawa, Y. Nojiri, A. Körtzinger, T. Steinhoff, M. Hoppema, J. Olafsson, T. S. Arnarson, B. Tilbrook, T. Johannessen, A. Olsen, R. Bellerby, C. S. Wong, B. Delille, N. R. Bates, H. J. W. de Baar, Climatological mean and decadal change in surface ocean pCO2, and net sea–air CO2 flux over the global oceans. *Deep Sea Research Part II: Topical Studies in Oceanography* **56**, 554–577 (2009).
2. C. L. Sabine, R. A. Feely, N. Gruber, R. M. Key, K. Lee, J. L. Bullister, R. Wanninkhof, C. S. Wong, D. W. R. Wallace, B. Tilbrook, F. J. Millero, T.-H. Peng, A. Kozyr, T. Ono, A. F. Rios, The Oceanic Sink for Anthropogenic CO_2. *Science (1979)* **305**, 367–371 (2004).
3. N. Gruber, D. Clement, B. R. Carter, R. A. Feely, S. van Heuven, M. Hoppema, M. Ishii, R. M. Key, A. Kozyr, S. K. Lauvset, C. Lo Monaco, J. T. Mathis, A. Murata, A. Olsen, F. F. Perez, C. L. Sabine, T. Tanhua, R. Wanninkhof, The oceanic sink for anthropogenic CO_2 from 1994 to 2007. *Science (1979)* **363**, 1193–1199 (2019).
4. S. Khatiwala, F. Primeau, T. Hall, Reconstruction of the history of anthropogenic CO2 concentrations in the ocean. *Nature* **462**, 346–349 (2009).
5. G. T. Chen, F. J. Millero, Gradual increase of oceanic CO2. *Nature 1979 277:5693* **277**, 205–206 (1979).
6. J. D. Müller, N. Gruber, B. Carter, R. Feely, M. Ishii, N. Lange, S. K. Lauvset, A. Murata, A. Olsen, F. F. Pérez, C. Sabine, T. Tanhua, R. Wanninkhof, D. Zhu, Decadal Trends in the Oceanic Storage of Anthropogenic Carbon From 1994 to 2014. *AGU Advances* **4** (2023).
7. E. T. Buitenhuis, T. Hashioka, C. Le Quéré, Combined constraints on global ocean primary production using observations and models. *Global Biogeochem Cycles* **27**, 847–858 (2013).
8. G. A. McKinley, A. R. Fay, N. S. Lovenduski, D. J. Pilcher, Natural Variability and Anthropogenic Trends in the Ocean Carbon Sink. *Ann Rev Mar Sci* **9**, 125–150 (2017).
9. S. C. Doney, V. J. Fabry, R. A. Feely, J. A. Kleypas, Ocean Acidification: The Other CO 2 Problem . *Ann Rev Mar Sci* **1**, 169–192 (2009).
10. J. C. Orr, V. J. Fabry, O. Aumont, L. Bopp, S. C. Doney, R. A. Feely, A. Gnanadesikan, N. Gruber, A. Ishida, F. Joos, R. M. Key, K. Lindsay, E. Maier-Reimer, R. Matear, P. Monfray, A. Mouchet, R. G. Najjar, G. K. Plattner, K. B. Rodgers, C. L. Sabine, J. L. Sarmiento, R. Schlitzer, R. D. Slater, I. J. Totterdell, M. F. Weirig, Y. Yamanaka, A. Yool, Anthropogenic ocean acidification over the twenty-first century and its impact on calcifying organisms. *Nature* **437**, 681–686 (2005).
11. J. E. Bauer, W. J. Cai, P. A. Raymond, T. S. Bianchi, C. S. Hopkinson, P. A. G. Regnier, The changing carbon cycle of the coastal ocean. *Nature* **504**, 61–70 (2013).
12. W.-J. Cai, R. A. Feely, J. M. Testa, M. Li, W. Evans, S. R. Alin, Y.-Y. Xu, G. Pelletier, A. Ahmed, D. J. Greeley, J. A. Newton, N. Bednaršek, Natural and Anthropogenic Drivers of Acidification in Large Estuaries. *Ann Rev Mar Sci* **13**, 23–55 (2021).
13. K. Fennel, J. M. Testa, Biogeochemical Controls on Coastal Hypoxia. *Ann Rev Mar Sci* **11**, 105–130 (2019).
14. W.-J. Cai, Estuarine and Coastal Ocean Carbon Paradox: CO 2 Sinks or Sites of Terrestrial Carbon Incineration? . *Ann Rev Mar Sci* **3**, 123–145 (2011).
15. M. Dai, J. Su, Y. Zhao, E. E. Hofmann, Z. Cao, W.-J. Cai, J. Gan, F. Lacroix, G. G. Laruelle, F. Meng, J. D. Müller, P. A. G. Regnier, G. Wang, Z. Wang, Carbon Fluxes in the Coastal Ocean: Synthesis, Boundary Processes, and Future Trends. *Annu Rev Earth Planet Sci* **50**, 593–626 (2022).
16. G. G. Laruelle, W. J. Cai, X. Hu, N. Gruber, F. T. Mackenzie, P. Regnier, Continental shelves as a variable but increasing global sink for atmospheric carbon dioxide. *Nat Commun* **9**, 1–11 (2018).
17. F. Lacroix, T. Ilyina, G. G. Laruelle, P. Regnier, Reconstructing the Preindustrial Coastal Carbon Cycle Through a Global Ocean Circulation Model: Was the Global Continental Shelf Already Both Autotrophic and a CO2 Sink? *Global Biogeochem Cycles* **35** (2021).
18. T. Bourgeois, J. C. Orr, L. Resplandy, J. Terhaar, C. Ethé, M. Gehlen, L. Bopp, Coastal-ocean uptake of anthropogenic carbon. *Biogeosciences* **13**, 4167–4185 (2016).
19. P. Regnier, P. Friedlingstein, P. Ciais, F. T. Mackenzie, N. Gruber, I. A. Janssens, G. G. Laruelle, R. Lauerwald, S. Luyssaert, A. J. Andersson, S. Arndt, C. Arnosti, A. V. Borges, A. W. Dale, A. Gallego-Sala, Y. Goddéris, N. Goossens, J. Hartmann, C. Heinze, T. Ilyina, F. Joos, D. E. Larowe, J. Leifeld, F. J. R.

Commented [LX1]: Our references are 18 more than required. (Main text reference 1:98, 99-end for the supplements)

Reference list should be a reasonable accounting of the critical literature supporting the conclusions of the paper. Ensure inclusion of a diverse set of authors. Do not include excess references. The suggested upper limit for research articles is 80 and for review articles 150.

Al

Commented [LX2R1]: Well It is suggested and I go over the paper again and found nothing can be taken out
In the maintext, we have 67 citations.
22 in methods.

Meysman, G. Munhoven, P. A. Raymond, R. Spahni, P. Suntharalingam, M. Thullner, Anthropogenic perturbation of the carbon fluxes from land to ocean. *Nat Geosci* **6**, 597–607 (2013).
20. P. Regnier, L. Resplandy, R. G. Najjar, P. Ciais, The land-to-ocean loops of the global carbon cycle. *Nature* **603**, 401–410 (2022).
21. W. J. van Hoek, J. Wang, L. Vilmin, A. H. W. Beusen, J. M. Mogollón, G. Müller, P. A. Pika, X. Liu, J. J. Langeveld, A. F. Bouwman, J. J. Middelburg, Exploring Spatially Explicit Changes in Carbon Budgets of Global River Basins during the 20th Century. *Environ Sci Technol* **55**, 16757–16769 (2021).
22. P. A. Raymond, S. K. Hamilton, Anthropogenic influences on riverine fluxes of dissolved inorganic carbon to the oceans. *Limnol Oceanogr Lett* **3**, 143–155 (2018).
23. W.-J. Cai, R. A. Feely, J. M. Testa, M. Li, W. Evans, S. R. Alin, Y.-Y. Xu, G. Pelletier, A. Ahmed, D. J. Greeley, J. A. Newton, N. Bednaršek, Natural and Anthropogenic Drivers of Acidification in Large Estuaries. *Ann Rev Mar Sci* **13**, 1–33 (2021).
24. Z. Xu, B. Wang, H. Li, J. Zhang, H. Jin, J. Chen, Elevated anthropogenic CO2 invasion and stimulated carbonate dissolution in the South China Sea Basin. *Mar Chem* **249** (2023).
25. C. T. A. Chen, S. L. Wang, W. C. Chou, D. D. Sheu, Carbonate chemistry and projected future changes in pH and CaCO3 saturation state of the South China Sea. *Mar Chem* **101**, 277–305 (2006).
26. A. Schneider, T. Tanhua, A. Krtzinger, D. W. R. Wallace, High anthropogenic carbon content in the eastern Mediterranean. *J Geophys Res Oceans* **115**, 12050 (2010).
27. R. A. Feely, S. R. Alin, B. Carter, N. Bednar, B. Hales, F. Chan, T. M. Hill, B. Gaylord, E. Sanford, R. H. Byrne, C. L. Sabine, D. Greeley, L. Juranek, Chemical and biological impacts of ocean acidification along the west coast of North America. doi: 10.1016/j.ecss.2016.08.043 (2016).
28. M. C. Arroyo, A. J. Fassbender, B. R. Carter, C. A. Edwards, J. Fiechter, A. Norgaard, R. A. Feely, Dissimilar Sensitivities of Ocean Acidification Metrics to Anthropogenic Carbon Accumulation in the Central North Pacific Ocean and California Current Large Marine Ecosystem. *Geophys Res Lett* **49** (2022).
29. B. R. Carter, R. A. Feely, R. Wanninkhof, S. Kouketsu, R. E. Sonnerup, P. C. Pardo, C. L. Sabine, G. C. Johnson, B. M. Sloyan, A. Murata, S. Mecking, B. Tilbrook, K. Speer, L. D. Talley, F. J. Millero, S. E. Wijffels, A. M. Macdonald, N. Gruber, J. L. Bullister, Pacific Anthropogenic Carbon Between 1991 and 2017. *Global Biogeochem Cycles* **33**, 597–617 (2019).
30. B. R. Carter, R. A. Feely, S. Mecking, J. N. Cross, A. M. Macdonald, S. A. Siedlecki, L. D. Talley, C. L. Sabine, F. J. Millero, J. H. Swift, A. G. Dickson, K. B. Rodgers, Two decades of Pacific anthropogenic carbon storage and ocean acidification along Global Ocean Ship-based Hydrographic Investigations Program sections P16 and P02. *Global Biogeochem Cycles* **31**, 306–327 (2017).
31. S. R. Pacella, C. A. Brown, G. G. Waldbusser, R. G. Labiosa, B. Hales, Seagrass habitat metabolism increases short-term extremes and long-term offset of CO2 under future ocean acidification. *Proceedings of the National Academy of Sciences* **115**, 3870–3875 (2018).
32. E. Simpson, D. Ianson, K. E. Kohfeld, Using End-Member Models to Estimate Seasonal Carbonate Chemistry and Acidification Sensitivity in Temperate Estuaries. *Geophys Res Lett* **49**, 1–12 (2022).
33. W. J. Cai, X. Hu, W. J. Huang, M. C. Murrell, J. C. Lehrter, S. E. Lohrenz, W. C. Chou, W. Zhai, J. T. Hollibaugh, Y. Wang, P. Zhao, X. Guo, K. Gundersen, M. Dai, G. C. Gong, Acidification of subsurface coastal waters enhanced by eutrophication. *Nat Geosci* **4**, 766–770 (2011).
34. R. Wanninkhof, L. Barbero, R. Byrne, W. J. Cai, W. J. Huang, J. Z. Zhang, M. Baringer, C. Langdon, Ocean acidification along the Gulf Coast and East Coast of the USA. *Cont Shelf Res* **98**, 54–71 (2015).
35. Y. Y. Xu, W. J. Cai, R. Wanninkhof, J. Salisbury, J. Reimer, B. Chen, Long-Term Changes of Carbonate Chemistry Variables Along the North American East Coast. *J Geophys Res Oceans* **125** (2020).
36. T.-H. Huang, W.-J. Cai, P. Vlahos, D. W. R. Wallace, E. R. Lewis, C.-T. A. Chen, The Mid-Atlantic Bight Dissolved Inorganic Carbon System Observed in the March 1996 DOE Ocean Margins Program (OMP)—A Baseline Study. *Front Mar Sci* **8**, 1–16 (2021).
37. Z. A. Wang, R. Wanninkhof, W. J. Cai, R. H. Byrne, X. Hu, T. H. Peng, W. J. Huang, The marine inorganic carbon system along the Gulf of Mexico and Atlantic coasts of the United States: Insights from a transregional coastal carbon study. *Limnol Oceanogr* **58**, 325–342 (2013).
38. D. F. Bumpus, A description of the circulation on the continental shelf of the east coast of the United States. *Prog Oceanogr* **6**, 111–157 (1973).
39. D. C. Chapman, R. C. Beardsley, On the Origin of Shelf Water in the Middle Atlantic Bight. *J Phys Oceanogr* **19**, 384–391 (1989).

40. M. Liu, T. Tanhua, Characteristics of Water Masses in the Atlantic Ocean based on GLODAPv2 data. *Ocean Science Discussions*, 1–43 (2019).
41. C. Romera-Castillo, J. Heras, M. Álvarez, X. A. Álvarez-Salgado, G. Mata, E. Sáenz-de-Cabezón, Application of multi-regression machine learning algorithms to solve ocean water mass mixing in the Atlantic Ocean. *Front Mar Sci* **9**, 1978 (2022).
42. K. Friis, A. Körtzinger, J. Pätsch, D. W. R. Wallace, On the temporal increase of anthropogenic CO2 in the subpolar North Atlantic. *Deep Sea Res 1 Oceanogr Res Pap* **52**, 681–698 (2005).
43. D. W. R. Wallace, *Monitoring Global Ocean Carbon Inventories* (Ocean Observing System Development Panel, College Station, Tex. :, 1995).
44. S. Minobe, A. Kuwano-Yoshida, N. Komori, S. P. Xie, R. J. Small, Influence of the Gulf Stream on the troposphere. *Nature 2008 452:7184* **452**, 206–209 (2008).
45. H. Stommel, *The Gulf Stream* (University of California Press, 1965; https://www.degruyter.com/document/doi/10.1525/9780520318564/html).
46. M. Rhein, D. Kieke, R. Steinfeldt, Advection of North Atlantic Deep Water from the Labrador Sea to the southern hemisphere. *J Geophys Res Oceans* **120**, 2471–2487 (2015).
47. S. C. Doney, J. L. Bullister, A chlorofluorocarbon section in the eastern North Atlantic. *Deep Sea Research Part A, Oceanographic Research Papers* **39**, 1857–1883 (1992).
48. D. M. Etheridge, L. P. Steele, R. L. Langenfelds, R. J. Francey, J. M. Barnola, V. I. Morgan, Natural and anthropogenic changes in atmospheric CO2 over the last 1000 years from air in Antarctic ice and firn. *Journal of Geophysical Research Atmospheres* **101**, 4115–4128 (1996).
49. J. Du, J. Shen, Water residence time in Chesapeake Bay for 1980–2012. *Journal of Marine Systems* **164**, 101–111 (2016).
50. G. Gildas Laruelle, N. Goossens, S. Arndt, W. J. Cai, P. Regnier, Air-water CO2 evasion from US East Coast estuaries. *Biogeosciences* **14**, 2441–2468 (2017).
51. W. G. Zhang, J. L. Wilkin, O. M. E. Schofield, Simulation of water age and residence time in New York Bight. *J Phys Oceanogr* **40**, 965–982 (2010).
52. J. R. Holmquist, L. Windham-Myers, B. Bernal, K. B. Byrd, S. Crooks, M. E. Gonneea, N. Herold, S. H. Knox, K. D. Kroeger, J. McCombs, J. P. Megonigal, M. Lu, J. T. Morris, A. E. Sutton-Grier, T. G. Troxler, D. E. Weller, Uncertainty in United States coastal wetland greenhouse gas inventorying. *Environmental Research Letters* **13** (2018).
53. P. I. Macreadie, M. D. P. Costa, T. B. Atwood, D. A. Friess, J. J. Kelleway, H. Kennedy, C. E. Lovelock, O. Serrano, C. M. Duarte, Blue carbon as a natural climate solution. *Nature Reviews Earth & Environment 2021 2:12* **2**, 826–839 (2021).
54. F. T. Mackenzie, A. Lerman, A. J. Andersson, Past and present of sediment and carbon biogeochemical cycling models. *Biogeosciences* **1**, 11–32 (2004).
55. A. V. Borges, B. Delille, M. Frankignoulle, Budgeting sinks and sources of CO2 in the coastal ocean: Diversity of ecosystems counts. *Geophys Res Lett* **32**, 1–4 (2005).
56. A. Lerman, F. T. Mackenzie, L. M. Ver, "Coupling of the Perturbed C-N-P Cycles in Industrial Time."
57. M. Li, Y. Guo, W.-J. Cai, J. M. Testa, C. Shen, R. Li, J. Su, Projected increase in carbon dioxide drawdown and acidification in large estuaries under climate change. *Communications Earth & Environment 2023 4:1* **4**, 1–10 (2023).
58. K. Lee, C. L. Sabine, T. Tanhua, T. W. Kim, R. A. Feely, H. C. Kim, Roles of marginal seas in absorbing and storing fossil fuel CO2. [Preprint] (2011). https://doi.org/10.1039/c0ee00663g.
59. A. Schneider, T. Tanhua, A. Krtzinger, D. W. R. Wallace, High anthropogenic carbon content in the eastern Mediterranean. *J Geophys Res Oceans* **115** (2010).
60. Y. W. Watanabe, J. Nishioka, T. Nakatsuka, Decadal time evolution of oceanic uptake of anthropogenic carbon in the Okhotsk Sea. *Geophys Res Lett* **40**, 322–326 (2013).
61. R. A. Feely, S. R. Alin, J. Newton, C. L. Sabine, M. Warner, A. Devol, C. Krembs, C. Maloy, The combined effects of ocean acidification, mixing, and respiration on pH and carbonate saturation in an urbanized estuary. *Estuar Coast Shelf Sci* **88**, 442–449 (2010).
62. A. Hare, W. Evans, K. Pocock, C. Weekes, I. Gimenez, Contrasting marine carbonate systems in two fjords in British Columbia, Canada: Seawater buffering capacity and the response to anthropogenic CO2 invasion. *PLoS One* **15** (2020).

63. P. St-Laurent, M. A. M. Friedrichs, R. G. Najjar, E. H. Shadwick, H. Tian, Y. Yao, Relative impacts of global changes and regional watershed changes on the inorganic carbon balance of the Chesapeake Bay. *Biogeosciences* **17**, 3779–3796 (2020).
64. T. S. Bianchi, L. M. Mayer, J. H. F. Amaral, S. Arndt, V. Galy, D. B. Kemp, S. A. Kuehl, N. J. Murray, P. Regnier, Anthropogenic impacts on mud and organic carbon cycling. Nature Research [Preprint] (2024). https://doi.org/10.1038/s41561-024-01405-5.
65. N. Gruber, D. C. E. Bakker, T. DeVries, L. Gregor, J. Hauck, P. Landschützer, G. A. McKinley, J. D. Müller, Trends and variability in the ocean carbon sink. Springer Nature [Preprint] (2023). https://doi.org/10.1038/s43017-022-00381-x.
66. T. Jarníková, D. Ianson, S. E. Allen, A. E. Shao, E. M. Olson, Anthropogenic Carbon Increase has Caused Critical Shifts in Aragonite Saturation Across a Sensitive Coastal System. *Global Biogeochem Cycles* **36** (2022).
67. J. Su, W. J. Cai, J. Brodeur, B. Chen, N. Hussain, Y. Yao, C. Ni, J. M. Testa, M. Li, X. Xie, W. Ni, K. M. Scaboo, Y. yuan Xu, J. Cornwell, C. Gurbisz, M. S. Owens, G. G. Waldbusser, M. Dai, W. M. Kemp, Chesapeake Bay acidification buffered by spatially decoupled carbonate mineral cycling. *Nat Geosci* **13**, 441–447 (2020).
68. J. Hauck, C. Völker, Rising atmospheric CO2 leads to large impact of biology on Southern Ocean CO2 uptake via changes of the Revelle factor. *Geophys Res Lett* **42**, 1459–1464 (2015).
69. L. Q. Jiang, R. A. Feely, R. Wanninkhof, D. Greeley, L. Barbero, S. Alin, B. R. Carter, D. Pierrot, C. Featherstone, J. Hooper, C. Melrose, N. Monacci, J. D. Sharp, S. Shellito, Y. Y. Xu, A. Kozyr, R. H. Byrne, W. J. Cai, J. Cross, G. C. Johnson, B. Hales, C. Langdon, J. Mathis, J. Salisbury, D. W. Townsend, Coastal Ocean Data Analysis Product in North America (CODAP-NA)-an internally consistent data product for discrete inorganic carbon, oxygen, and nutrients on the North American ocean margins. *Earth Syst Sci Data* **13**, 2777–2799 (2021).
70. X. Li, Y. Xu, D. L. Kirchman, W. Cai, Carbonate Parameter Estimation and Its Application in Revealing Temporal and Spatial Variation in the South and Mid-Atlantic Bight, USA. *J Geophys Res Oceans* **127**, e2022JC018811 (2022).
71. J. L. Sarmiento, J. C. Orr, U. Siegenthaler, A perturbation simulation of CO2 uptake in an ocean general circulation model. *J Geophys Res* **97**, 3621–3645 (1992).
72. B. I. McNeil, R. J. Matear, The non-steady state oceanic CO2 signal: Its importance, magnitude and a novel way to detect it. *Biogeosciences* **10**, 2219–2228 (2013).
73. D. Clement, N. Gruber, The eMLR(C*) Method to Determine Decadal Changes in the Global Ocean Storage of Anthropogenic CO2. *Global Biogeochem Cycles* **32**, 654–679 (2018).
74. T. Takahashi, Global air-sea flux of CO2 based on surface ocean pCO2, and seasonal biological and temperature effects. *Deep-Sea Research Part II* **49**, 1601–1622 (2002).
75. R. Wanninkhof, S. C. Doney, J. L. Bullister, N. M. Levine, M. Warner, N. Gruber, Detecting anthropogenic CO2 changes in the interior Atlantic Ocean between 1989 and 2005. *J Geophys Res Oceans* **115**, 1–25 (2010).
76. P. J. Brown, D. C. E. Bakker, U. Schuster, A. J. Watson, Anthropogenic carbon accumulation in the subtropical North Atlantic. *J Geophys Res Oceans* **115**, 1–20 (2010).
77. R. J. Woosley, F. J. Millero, R. Wanninkhof, Rapid anthropogenic changes in CO_2 and pH in the Atlantic Ocean: 2003-2014. *Global Biogeochem Cycles* **30**, 70–90 (2016).
78. S. R. Alin, R. A. Feely, A. G. Dickson, J. Martín Hernández-Ayón, L. W. Juranek, M. D. Ohman, R. Goericke, Robust empirical relationships for estimating the carbonate system in the southern California Current System and application to CalCOFI hydrographic cruise data (2005-2011). *J Geophys Res Oceans* **117** (2012).
79. L. W. Juranek, R. A. Feely, W. T. Peterson, S. R. Alin, B. Hales, K. Lee, C. L. Sabine, J. Peterson, A novel method for determination of aragonite saturation state on the continental shelf of central Oregon using multi-parameter relationships with hydrographic data. *Geophys Res Lett* **36**, L24601 (2009).
80. T.-W. Kim, K. Lee, R. A. Feely, C. L. Sabine, C.-T. A. Chen, H. J. Jeong, K. Y. Kim, Prediction of Sea of Japan (East Sea) acidification over the past 40 years using a multiparameter regression model. *Global Biogeochem Cycles* **24**, n/a-n/a (2010).

81. K. McGarry, S. A. A. Siedlecki, J. Salisbury, S. R. R. Alin, Multiple linear regression models for reconstructing and exploring processes controlling the carbonate system of the northeast US from basic hydrographic data. *J Geophys Res Oceans* **126**, 1–19 (2020).
82. N. L. Williams, L. W. Juranek, K. S. Johnson, R. A. Feely, S. C. Riser, L. D. Talley, J. L. Russell, J. L. Sarmiento, R. Wanninkhof, Empirical algorithms to estimate water column pH in the Southern Ocean. *Geophys Res Lett* **43**, 3415–3422 (2016).
83. S. R. Signorini, A. Mannino, R. G. Najjar, M. A. M. Friedrichs, W. J. Cai, J. Salisbury, Z. A. Wang, H. Thomas, E. Shadwick, Surface ocean pCO2 seasonality and sea-air CO2 flux estimates for the North American east coast. *J Geophys Res Oceans* **118**, 5439–5460 (2013).
84. C. L. Sabine, R. A. Feely, F. J. Millero, A. G. Dickson, C. Langdon, S. Mecking, D. Greeley, Decadal changes in Pacific carbon. *J Geophys Res Oceans* **113**, 1–12 (2008).
85. N. F. Goodkin, N. M. Levine, S. C. Doney, R. Wanninkhof, Impacts of temporal CO 2 and climate trends on the detection of ocean anthropogenic CO 2 accumulation. *Global Biogeochem Cycles* **25** (2011).
86. Y. Plancherel, K. B. Rodgers, R. M. Key, A. R. Jacobson, J. L. Sarmiento, Climate of the Past Geoscientific Instrumentation Methods and Data Systems Role of regression model selection and station distribution on the estimation of oceanic anthropogenic carbon change by eMLR. *Biogeosciences* **10**, 4801–4831 (2013).
87. B. R. Carter, N. L. Williams, A. R. Gray, R. A. Feely, Locally interpolated alkalinity regression for global alkalinity estimation. *Limnol Oceanogr Methods* **14**, 268–277 (2016).
88. B. R. Carter, R. A. Feely, N. L. Williams, A. G. Dickson, M. B. Fong, Y. Takeshita, Updated methods for global locally interpolated estimation of alkalinity, pH, and nitrate. *Limnol Oceanogr Methods* **16**, 119–131 (2018).
89. J. S. T. Forsyth, M. Andres, G. G. Gawarkiewicz, Recent accelerated warming of the continental shelf off New Jersey: Observations from the CMV Oleander expendable bathythermograph line. *J Geophys Res Oceans* **120**, 2370–2384 (2015).
90. E. J. Wallace, L. B. Looney, D. Gong, "Multi-decadal trends and variability in temperature and salinity in Multi-decadal trends and variability in temperature and salinity in the Mid-Atlantic Bight, Georges Bank, and Gulf of Maine the Mid-Atlantic Bight, Georges Bank, and Gulf of Maine Multi-decadal trends and variability in temperature and salinity in the Mid-Atlantic Bight, Georges Bank, and Gulf of Maine" (2018); https://scholarworks.wm.edu/vimsarticles/1860.
91. R. J. Woosley, F. J. Millero, Freshening of the western Arctic negates anthropogenic carbon uptake potential. *Limnol Oceanogr* **65**, 1834–1846 (2020).
92. A. Joesoef, W.-J. Huang, Y. Gao, W.-J. Cai, Air–water fluxes and sources of carbon dioxide in the Delaware Estuary: spatial and seasonal variability. *Biogeosciences* **12**, 6085–6101 (2015).
93. R. B. Wallace, H. Baumann, J. S. Grear, R. C. Aller, C. J. Gobler, Coastal ocean acidification: The other eutrophication problem. *Estuar Coast Shelf Sci* **148**, 1–13 (2014).
94. R. Wanninkhof, Relationship between wind speed and gas exchange over the ocean revisited. *Limnol Oceanogr Methods* **12**, 351–362 (2014).
95. R. F. Weiss, Carbon dioxide in water and seawater: the solubility of a non-ideal gas. *Mar Chem* **2**, 203–215 (1974).
96. Y. Y. Xu, W. J. Cai, Y. Gao, R. Wanninkhof, J. Salisbury, B. Chen, J. J. Reimer, S. Gonski, N. Hussain, Short-term variability of aragonite saturation state in the central Mid-Atlantic Bight. *J Geophys Res Oceans* **122**, 4274–4290 (2017).
97. S. Van Heuven, D. Pierrot, J. W. B. Rae, E. Lewis, D. W. R. Wallace, MATLAB Program Developed for CO2 System Calculations. ORNL/CDIAC-105b. Carbon Dioxide Information Analysis Center (CDIAC) [Preprint] (2011). https://doi.org/https://cdiac.ess-dive.lbl.gov/ftp/co2sys/CO2SYS_calc_MATLAB_v1.1/1.
98. A. V. Borges, Do we have enough pieces of the jigsaw to integrate CO2 fluxes in the coastal ocean? *Estuaries* **28**, 3–27 (2005).
99. B. I. McNeil, R. J. Matear, The non-steady state oceanic CO2 signal: Its importance, magnitude and a novel way to detect it. *Biogeosciences* **10**, 2219–2228 (2013).
100. R. F. Keeling, Comment on "The Ocean Sink for Anthropogenic CO2." *Science (1979)* **308** (2005).
101. B. I. Mcneil, R. J. Matear, Climate of the Past Geoscientific Instrumentation Methods and Data Systems The non-steady state oceanic CO 2 signal: its importance, magnitude and a novel way to detect it. *Biogeosciences* **10**, 2219–2228 (2013).

102. X. Liu, J. P. Dunne, C. A. Stock, M. J. Harrison, A. Adcroft, L. Resplandy, Simulating Water Residence Time in the Coastal Ocean: A Global Perspective. *Geophys Res Lett* **46**, 13910–13919 (2019).
103. P. G. Brewer, Direct observation of the oceanic CO2 increase. *Geophys Res Lett* **5**, 997–1000 (1978).
104. N. Gruber, Anthropogenic CO2 in the Atlantic Ocean. *Global Biogeochem Cycles* **12**, 165–191 (1998).
105. D. W. Waugh, T. M. Hall, B. I. Mcneil, R. Key, R. J. Matear, Anthropogenic CO2 in the oceans estimated using transit time distributions. *Tellus B Chem Phys Meteorol* **58**, 376–389 (2006).
106. C. L. Sabine, T. Tanhua, Estimation of Anthropogenic CO $_2$ Inventories in the Ocean. *Ann Rev Mar Sci* **2**, 175–198 (2010).
107. N. F. Goodkin, N. M. Levine, S. C. Doney, R. Wanninkhof, Impacts of temporal CO 2 and climate trends on the detection of ocean anthropogenic CO 2 accumulation. **25**, 1–11 (2011).
108. B. Chen, W. J. Cai, J. R. Brodeur, N. Hussain, J. M. Testa, W. Ni, Q. Li, Seasonal and spatial variability in surface pCO2 and air–water CO2 flux in the Chesapeake Bay. *Limnol Oceanogr* **65**, 3046–3065 (2020).
109. I. Semiletov, I. Pipko, Ö. Gustafsson, L. G. Anderson, V. Sergienko, S. Pugach, O. Dudarev, A. Charkin, A. Gukov, L. Bröder, A. Andersson, E. Spivak, N. Shakhova, Acidification of East Siberian Arctic Shelf waters through addition of freshwater and terrestrial carbon. *Nature Geoscience 2016 9:5* **9**, 361–365 (2016).
110. D. C. E. Bakker, B. Pfeil, C. S. Landa, N. Metzl, K. M. O'Brien, A. Olsen, K. Smith, C. Cosca, S. Harasawa, S. D. Jones, S. I. Nakaoka, Y. Nojiri, U. Schuster, T. Steinhoff, C. Sweeney, T. Takahashi, B. Tilbrook, C. Wada, R. Wanninkhof, S. R. Alin, C. F. Balestrini, L. Barbero, N. R. Bates, A. A. Bianchi, F. Bonou, J. Boutin, Y. Bozec, E. F. Burger, W. J. Cai, R. D. Castle, L. Chen, M. Chierici, K. Currie, W. Evans, C. Featherstone, R. A. Feely, A. Fransson, C. Goyet, N. Greenwood, L. Gregor, S. Hankin, N. J. Hardman-Mountford, J. Harlay, J. Hauck, M. Hoppema, M. P. Humphreys, C. W. Hunt, B. Huss, J. S. P. Ibánhez, T. Johannessen, R. Keeling, V. Kitidis, A. Körtzinger, A. Kozyr, E. Krasakopoulou, A. Kuwata, P. Landschützer, S. K. Lauvset, N. Lefèvre, C. lo Monaco, A. Manke, J. T. Mathis, L. Merlivat, F. J. Millero, P. M. S. Monteiro, D. R. Munro, A. Murata, T. Newberger, A. M. Omar, T. Ono, K. Paterson, D. Pearce, D. Pierrot, L. L. Robbins, S. Saito, J. Salisbury, R. Schlitzer, B. Schneider, R. Schweitzer, R. Sieger, I. Skjelvan, K. F. Sullivan, S. C. Sutherland, A. J. Sutton, K. Tadokoro, M. Telszewski, M. Tuma, S. M. A. C. van Heuven, D. Vandemark, B. Ward, A. J. Watson, S. Xu, A multi-decade record of high-quality fCO2 data in version 3 of the Surface Ocean CO2 Atlas (SOCAT). *Earth Syst Sci Data* **8**, 383–413 (2016).
111. T. Takahashi, S. C. Sutherland, A. Kozyr, Global Ocean Surface Water Partial Pressure of CO2 Database (LDEO Database Version 2019): Measurements Performed During 1957-2019 (NCEI Accession 0160492). *NOAA National Centers for Environmental Information* (2020).
112. B. R. Carter, N. L. Williams, W. Evans, A. J. Fassbender, L. Barbero, C. Hauri, R. A. Feely, A. J. Sutton, Time of Detection as a Metric for Prioritizing Between Climate Observation Quality, Frequency, and Duration. *Geophys Res Lett* **46**, 3853–3861 (2019).
113. A. J. Sutton, C. L. Sabine, R. A. Feely, W. J. Cai, M. F. Cronin, M. J. McPhaden, J. M. Morell, J. A. Newton, J. H. Noh, S. R. Ólafsdóttir, J. E. Salisbury, U. Send, D. C. Vandemark, R. A. Weller, Using present-day observations to detect when anthropogenic change forces surface ocean carbonate chemistry outside preindustrial bounds. *Biogeosciences* **13**, 5065–5083 (2016).
114. J. B. Palter, M. S. Lozier, R. T. Barber, The effect of advection on the nutrient reservoir in the North Atlantic subtropical gyre. *Nature* **437**, 687–692 (2005).
115. J. Heiderich, R. E. Todd, Along-Stream Evolution of Gulf Stream Volume Transport. *J Phys Oceanogr* **50**, 2251–2270 (2020).
116. Z. B. Szuts, C. S. Meinen, Florida Current Salinity and Salinity Transport: Mean and Decadal Changes. *Geophys Res Lett* **44**, 10,495-10,503 (2017).
117. D. Kieke, I. Yashayaev, Studies of Labrador Sea Water formation and variability in the subpolar North Atlantic in the light of international partnership and collaboration. *Prog Oceanogr* **132**, 220–232 (2015).
118. A. G. Dickson, C. L. Sabine, J. R. Christian, *Guide to Best Practices for Ocean CO2 Measurements. PICES Special Publication* (2007)vol. 3.

Acknowledgments

The fieldwork and synthesis have been continuously supported by the National Oceanic and Atmospheric Administration's (NOAA) Ocean Acidification Program (OAP) over the past two decades. We thank captains and crew of all vessels involved in collecting the data at sea and the outstanding technical staff, students, postdocs, and PIs at NOAA and partner labs for their collaboration on the NOAA ocean acidification cruises. In particular, we thank Dr. Joseph Salisbury, Dr. Chris Langdon, and Dr. Rik Wanninkhof for contributing hydrographic, dissolved O_2, and DIC data and data quality assurance/ quality control. Dr. Ernie Lewis and Dr. Douglas Wallace are thanked for their contribution in collecting the DIC and other data during the 1996 Ocean Margin Program (OMP). We also thank Dr. Rik Wanninkhof, Dr. Richard Feely and Dr. Brendan Carter for reading early versions of this manuscript and providing insightful suggestions and comments.

Funding:

This work was supported by
National Oceanic and Atmospheric Administration grant NA16NOS0120020 (W-JC).
National Oceanic and Atmospheric Administration grant NA21NOS0120096 (W-JC)
National Science Foundation grant OCE2123768 (W-JC)

Author contributions: Conceptualization: WJC, XL; Methodology and analysis: XL, ZW; Visualization: XL; Supervision: WJC; Writing—original draft: XL; Writing—review & editing: WJC, ZO, ZW

Competing interests: Authors declare that they have no competing interests.

Data and materials availability: The discrete bottle data of Gulf of Mexico and East Coast Carbon cruise and East Coast Ocean Acidification cruises can be found in https://www.ncei.noaa.gov/access/ocean-carbon-acidification-data-system/synthesis/NAcruises.html. All other model details are available in the main text or the supplementary materials.

Figures and Tables

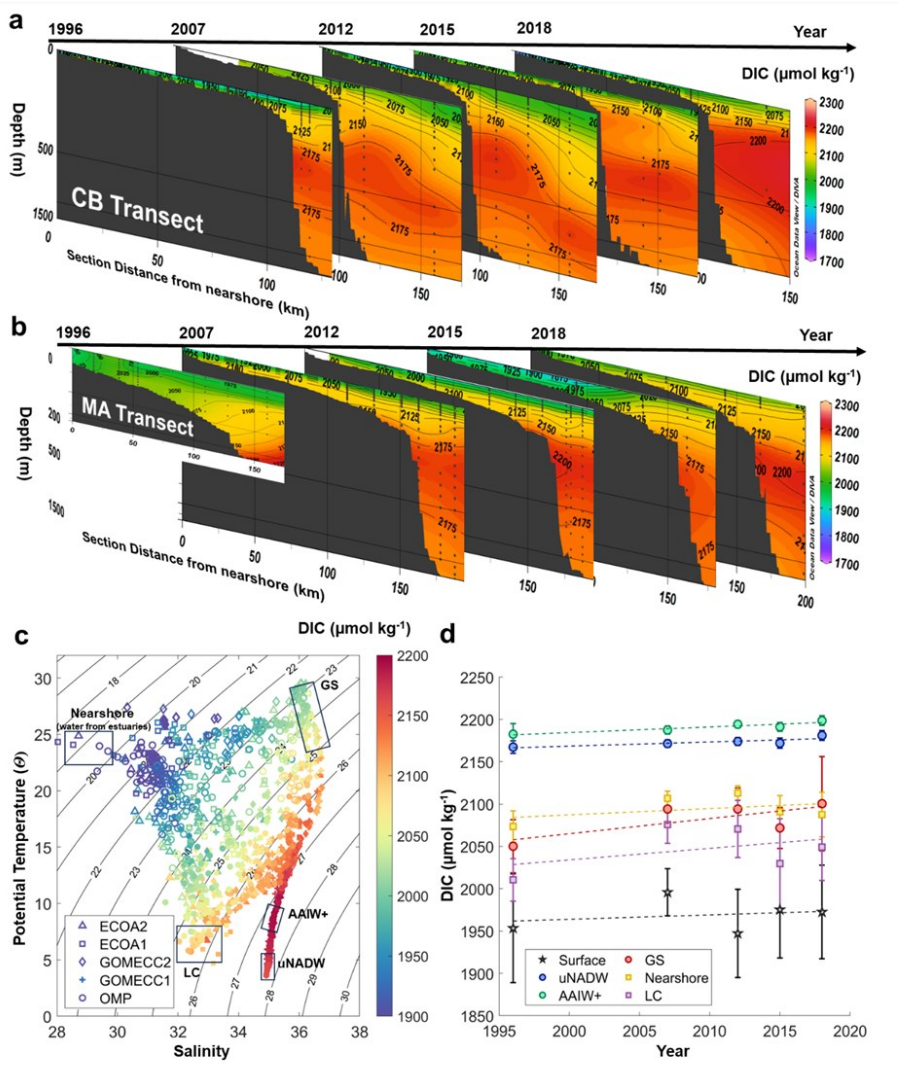

Fig. 1. Dissolved inorganic carbon (DIC) spatial distributions and decadal changes. The depth profiles of DIC in the most southern transect (**A**) Chesapeake Bay (CB) and the most northern (**B**) Massachusetts (MA) transect were exactly repeated in all five cruises from 1996 to 2018. DIC content increases from nearshore to offshore and increases with depth. The temperature and salinity diagram (**C**) reveals the major water masses with distinct DIC content. On the shelf, the nearshore The DIC content in the water column increases with time (**D**), especially in the off-slope top 200 m of Gulf Stream (GS) water (fig. S1).

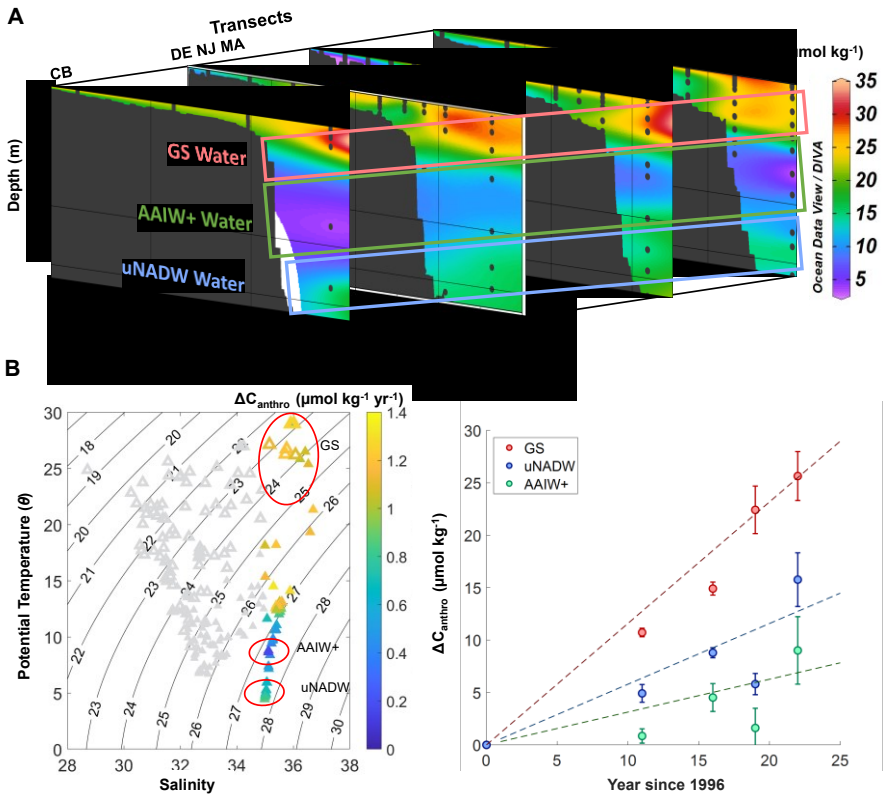

Figure 2. Slope water ΔC_{anthro} accumulation and increasing rate in different water masses. **(a)** The vertical spatial distribution of ΔC_{anthro} between 1996 - 2018 is listed from the north to the south (right to left): Massachusetts Transect (MA), New Jersey Transect (NJ), Delaware Transect (DE), and Chesapeake Bay Transect (CB). **(b)** The slope water ΔC_{anthro} increasing rates between 1996 -2018 overlay on the salinity-temperature diagram. Slope water is colored by ΔC_{anthro} increasing rate while the shelf water is in grey. The hollow triangles are surface water (< 20 m) while the solid ones are subsurface water (> 20 m). (**c**) The time series analysis of the increased ΔC_{anthro} (relative to 1996) in Gulf Steam (GS) water, upper North Atlantic Deep Water (uNADW), and Antarctic and other intermediate water (AAIW+). The dashed lines are linear regressions of ΔC_{anthro} against time in different water masses (regression coefficients in Table S6).

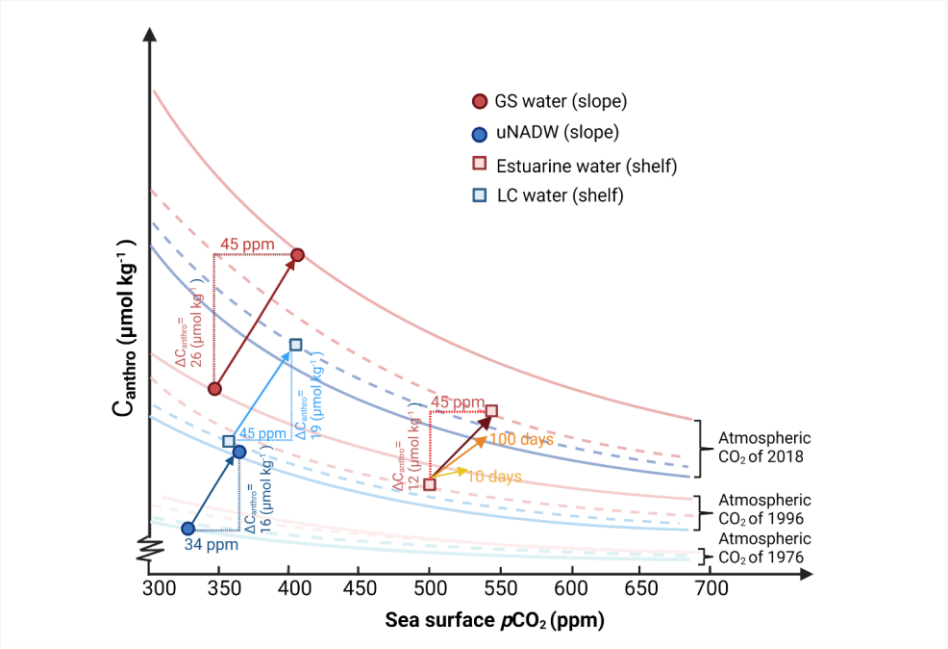

Figure 3. Schematic representation of ΔC_{anthro} accumulation mechanism in the coastal ocean. This C_{anthro} – sea surface pCO_2 (pCO_{2sw}) space was plotted with the assumption that the air-sea pCO_2 gradient has remained constant over the recent few decades. Three groups of contours are the C_{anthro} accumulation at the atmospheric CO_2 level of 1976, 1996, and 2018, respectively. In each group, the contours of different colors and line styles are C_{anthro} of slope GS water with average properties of S = 36, T = 25 °C, and TA = 2350 µmol kg^{-1} (red solid line), uNADW (blue solid line, S = 35, T = 5 °C, and TA = 2300 µmol kg^{-1}), nearshore water from estuaries (red dash line, S = 30, T = 20°C, TA = 2000 µmol kg^{-1}), and LC water (blue dash line, at S = 33, T =10°C, TA =2200 µmol kg^{-1}), respectively. The symbols and arrows represent the ΔC_{anthro} evolution in different waters. The ΔC_{anthro} accumulation of slope water (round circles and solid contours) depends on the water mass properties and water-mass age. The ΔC_{anthro} accumulation of shelf water (squares, dashed contours) is closely related to water chemical properties and water residence time (100 days, orange arrow and 10 days, yellow arrows). See more details in Method.

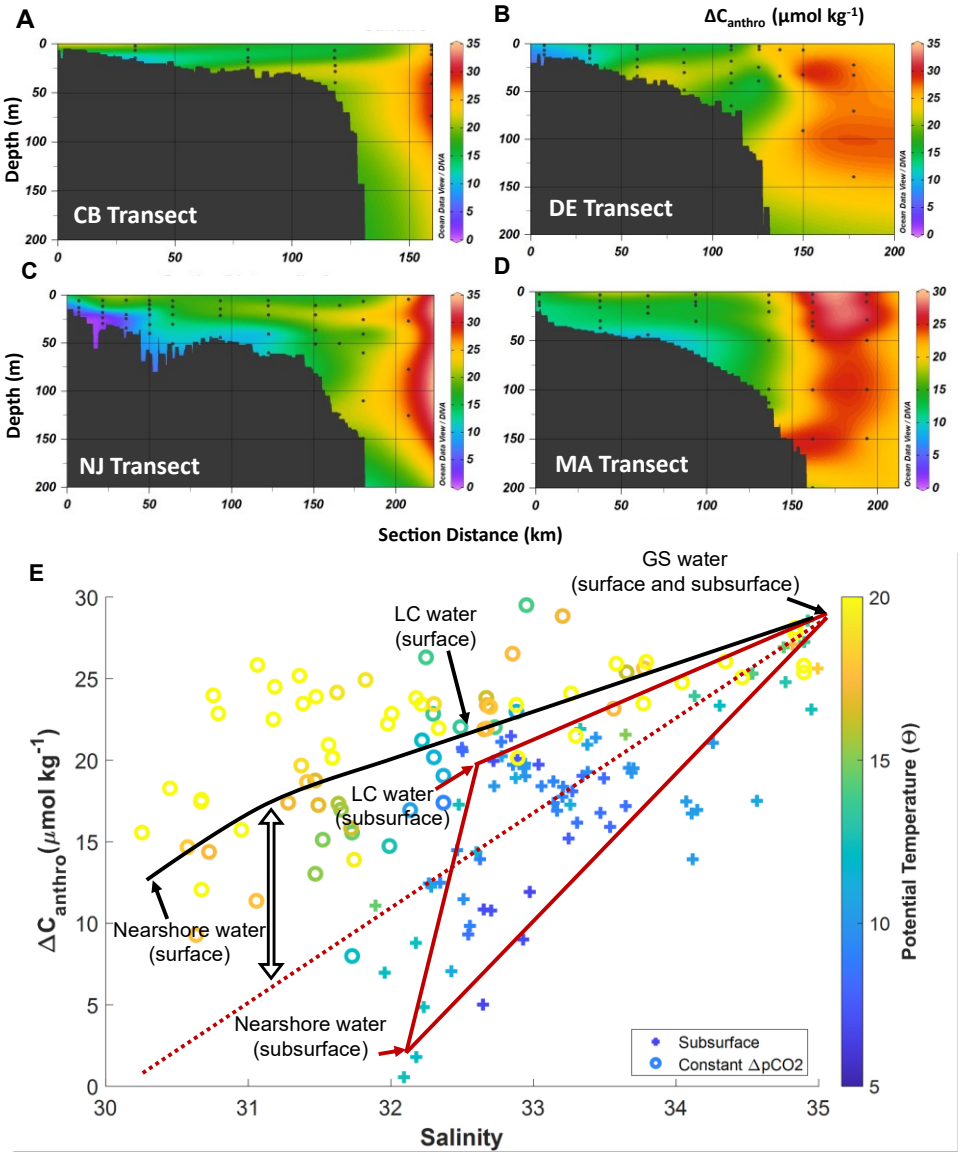

Figure 4. Shelf water ΔC_{anthro} spatial distribution and increasing rate between 1996 and 2018. The profile distribution of ΔC_{anthro} between 1996 and 2018 in (**a**) CB, (**b**) DE, (**c**) NJ, and (**d**) MA transect reveals a decreasing ΔC_{anthro} from the offshore to the nearshore. (**e**) The relationship between salinity and ΔC_{anthro} in the subsurface ("+" symbol) indicates a three-endmember mixing (denoted by the red triangle) of GS water, LC water, and nearshore water

from estuaries. The surface water ΔC_{anthro} accumulation rates are estimated by the constant ΔpCO_2 method ("○" symbol). The red dashed line is the average of subsurface ΔC_{anthro} by salinity and extrapolated to the S = 30, which can be considered as a composite mixing line of the open ocean end-member and a composite low salinity end-member. The black line is the average of surface ΔC_{anthro}. The differences between the two (as the black hollow arrow indicates) are assigned as the accumulated ΔC_{anthro} from the locally CO_2 uptake on the shelf.

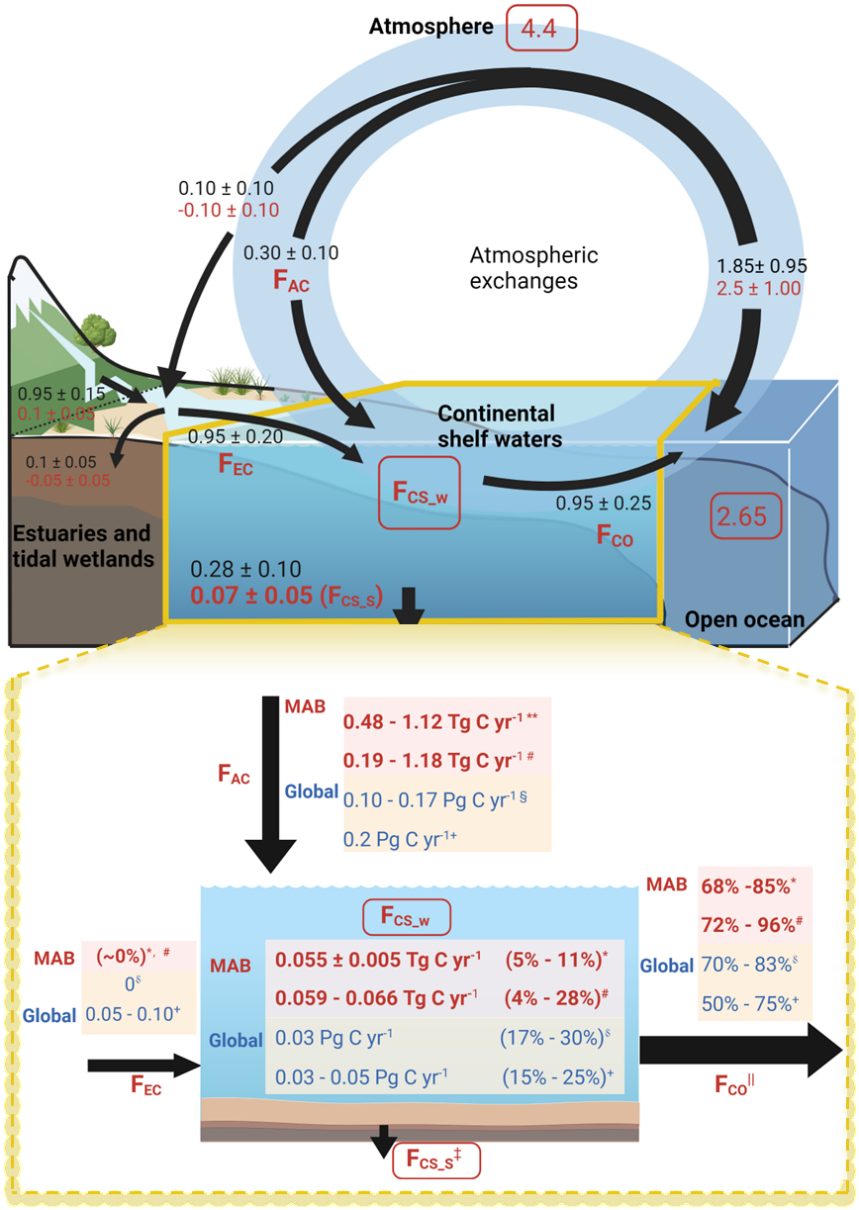

Fig. 5 The C_{anthro} budgets of the Land to Ocean Aquatic Continuum (LOAC) loop model in the MAB and global coastal region. (a) The concepts of LOAC is adapted from Regnier et al.,

(2022) and the yellow box indicates our research area, the continental shelf water, while the light blue (left box) and dark blue (right box) indicate the estuaries-wetland box and open ocean box, respectively. The numbers in black are present carbon flux from Regnier et al., (2022). The unit is PgC yr^{-1}. The red number or flux (F) indicates anthropogenic perturbations. F_{EC} represents the anthropogenic flux from estuaries to continental shelf; F_{AC} from atmosphere to continental shelf; F_{CO} from continental shelf to ocean. F_{CS} is the C_{anthro} accumulated in the continental shelf box. (b) The C_{anthro} flux (F) and export percentage of the continental shelf box derived from this research in the MAB (red numbers) and from other models or synthesis in global scale (blue numbers). Here we further divided F_{CS} into the C_{anthro} accumulated in the water column (F_{CS_W}) and buried in sediments (F_{CS_S}).

* Observational results from this study. ** The C_{anthro} air-sea gas flux is assumed to be ~ 30% - 70% of the total air-sea flux (1.6± 0.3 Tg C yr^{-1}) (*15*, *18*, *20*, *54*, *55*)

One dimensional box model from this study based on different water residence time (10d, 20d, 50d, 100d). Details of the model are in the Methods.

ᵹ Global ocean general circulation and biogeochemistry model (Nucleus for European Modelling of the Ocean, Pelagic Interaction Scheme for Carbon and Ecosystem Studies) from Bourgeois et al(*18*) § 0.17 Pg C yr^{-1} is from Borges 2005(*98*)

\+ Global coastal ocean flux and budget based on data synthesis of published work from Regnier et al 2013(*19*) and Regnier et al 2022(*20*)

‡ In our MAB study (*), we assume the perturbed particulate organic carbon flux (F_{CS_S}) is about the twice of the C_{anthro} in the water column (F_{CS_W}) (*17*, *20*, *56*) as the global synthesis by Regnier et al 2022(*20*) (+). In the model studies (# and ᵹ) , POC is not taken into consideration.

|| $F_{co} = F_{AC} + F_{EC} - F_{CS}$, where $F_{CS} = F_{CS\_W} + F_{CS\_S}$